A hybrid lattice Boltzmann - Navier-Stokes method for unsteady aerodynamic and aeroacoustic computations

Alexandre Suss, Ivan Mary, Thomas Le Garrec, Simon Marié

A hybrid lattice Boltzmann - Navier-Stokes method for unsteady aerodynamic and aeroacoustic computations

Alexandre Suss[1,*], Ivan Mary[1], Thomas Le Garrec[1], Simon Marié[2,3]

[1] *DAAA, ONERA, Université Paris Saclay, F-92322 Châtillon - France*
[2] *Laboratoire DynFluid, F-75013 Paris - France*
[3] *Conservatoire National des Arts et Métiers, F-75003 Paris - France*

Abstract

A hybrid numerical method coupling the standard lattice Boltzmann method (LBM) and a compressible finite-volume Navier-Stokes (NS) solver is proposed in the context of unsteady aerodynamic and aeroacoustic simulations. The trend being towards more realistic and detailed simulations in a reasonable amount of CPU time, lattice Boltzmann and Navier-Sokes solvers can be combined to solve the same problem. The present hybrid method relies on a zonal decomposition of the computational domain thus allowing to exploit the numerical features of both methods to their optimal extent in specific flow regions.

The key issue when combining the LBM with a Navier-Stokes solver is to ensure a smooth transition of the flow variables at the two-way coupling interface. While existing approaches consider overlapping meshes, a direct grid coupling is here derived. The mapping from the macroscopic flow variables to the set of lattice Boltzmann distribution functions is performed analytically thanks to a Chapman-Enskog expansion and draws a direct link to advanced regularised collision operators. Unsteady computations are enabled by coupling the lattice Boltzmann stream and collide algorithm with explicit and implicit Navier-Stokes time-stepping schemes. The hybrid method is then assessed on four time-dependent test cases representative of aerodynamic and aeroacoustic problems. The proposed approach is proven to yield very accurate results while keeping the numerical advantages of both methods and reducing the overall computational cost of direct noise computations.

Keywords: Lattice Boltzmann Method, Navier-Stokes equations, Finite-Volume, Coupling, Aerodynamics, Computational Aeroacoustics

1. Introduction

Computational Fluid Dynamics (CFD) has become an important tool in aerospace sciences enabling both researchers and engineers to get more insight into complex fluid phenomena and drastically decrease

*Corresponding author.
Email address: alexandre.suss@onera.fr (Alexandre Suss)

aircraft development lead-time [1]. Nowadays, Reynolds-Averaged Navier-Stokes (RANS) simulations on body-fitted meshes are of common practice in the industry since computations can easily be carried out overnight. However, RANS solutions, which rely on the modelling of all turbulent scales, are unreliable if complex turbulent phenomena occur or if aeroacoustics have to be finely characterised. As a consequence, the ability to perform accurate broadband three-dimensional unsteady flow simulations such as Large Eddy Simulations (LES) in reasonable computational time is a crucial issue.

In his 2019 review paper, Löhner [2] suggested that structured finite-type Navier-Stokes methods or lattice Boltzmann methods might be the most promising ones to achieve industrial level LES simulations in the next few years. On one hand, LES or hybrid RANS-LES applied to the Navier-Stokes equations are established approaches to describe the behavior of turbulent flows involving complex geometries [3]. Nevertheless, Navier-Stokes finite-type methods intrinsically suffer from numerical dissipation and thus face some difficulties to accurately predict the transport of turbulence over long distances and far-field acoustics. On the other hand, the lattice Boltzmann method (LBM) [4, 5, 6] which relies on a mesoscopic description of collisions between fluid particles, has gained an increasing amount of attention in the last decades. Indeed, the LBM appears as a good candidate for capturing the small acoustic pressure fluctuations thanks to its low dissipative properties [7]. Moreover, the LBM also provides the advantage of having a lower computational cost per mesh point with respect to traditional Navier-Stokes methods [7]. In light of these advantages, its range of applicability in both physics and engineering has grown in such a way that it enabled the simulation of a variety of very complex phenomena in aeronautics [8, 9, 10]. However, the standard lattice Boltzmann models still suffer from some limitations such as their restriction to low compressible isothermal flows and, by construction, their restriction to Cartesian grids and explicit time-stepping at constant CFL number. Consequently, the computation of wall-resolved turbulent boundary layers within the lattice Boltzmann framework remains costly and, despite their lack of generality and modeling errors [11], the use of wall-models is of common practice. Hence, in near-wall flow regions, solving a discretised form of the Navier-Stokes equations might outperform the LBM benefiting from their great flexibility through the use of body-fitted anisotropic meshes or implicit time-stepping. In other words, depending on the nature of the flow region, optimal efficiency may be reached with a different solver.

Following this idea, few hybrid lattice Boltzmann - Navier-Stokes methods for fluid problems have been proposed over the years. As indicated in a recent review [12], they are all based on a state-exchange with overlapping regions where both macroscopic and mesoscopic variables are computed. The key issue when coupling both solvers is to understand how the lattice Boltzmann set of variables is related to the Navier-Stokes one and conversely. Going from the LBM variables to the macroscopic ones is naturally offered by the statistical moments of distribution functions. However, the inverse mapping is not univocal as the distribution functions outnumber the macroscopic variables. The first coupling between the lattice Boltzmann

method and an incompressible finite-difference Navier-Stokes solver for fluid problems was introduced by Latt *et al.* [13] following the theoretical basis of Albuquerque *et al.* [14]. They proposed to use a Chapman-Enskog expansion leading to analytical passage relations between macroscopic quantities and distribution functions. Despite the fact that some restrictive assumptions were made in the Chapman-Enskog expansion by neglecting high-order terms and temporal derivatives, the method was validated on a $2D$ steady Poiseuille flow. Later, Luan *et al.* [15] introduced a coupled lattice Boltzmann - finite-volume Navier-Stokes method for convective heat transfer and incompressible fluid dynamics problems. The originality of their work relies in a reconstruction procedure specifically designed for the BGK collision operator [16]. However, in their strategy, the lattice Boltzmann method was used in near-wall regions, thus leading to an inadequate resolution of the boundary layer around a NACA0012 airfoil due to modelling errors [17]. Moreover, some discontinuities in the vicinity of the coupling interfaces have been evidenced in both the vorticity and pressure fields at steady state. They were expected to be caused by the weak compressibility and unsteady nature of the LBM compared to the incompressible and steady Navier-Stokes solver used in their study. To overcome the lack of generality in the prior study, Tong *et al.* [18] introduced a generalised reconstruction operator but still neglected high-order derivatives of distribution functions without any rigorous explanation. Their methodology was the first to be applied on unsteady fluid flow problems and relied on lattice Boltzmann sub-iterations in order to damp out potential spurious pressure oscillations. At the same time, Neumann *et al.* [19, 20, 21] also developed a steady and unsteady hybrid lattice Boltzmann – Navier-Stokes method using another macro-to-meso mapping strategy. Indeed, in their approach, the distribution functions are sought as solutions of an optimisation problem under conservation constraints. Despite promising results in the steady case [20], the extension to unsteady test cases was found to lead to compressibility errors large enough to severely perturb both the pressure and velocity field in the whole computational domain [21].

The present work follows the path paved by Albuquerque and Latt [13, 14] and further extends it to the simulation of unsteady flows. To ensure continuous pressure and vorticity fields, it is proposed to couple two compressible flow solvers, one relying on a finite-volume discretisation of the Navier-Stokes equations and another one based on the standard lattice Boltzmann method. The proposed coupling procedure does not require overlapping between the solvers and is introduced in a general context without any restrictive assumptions on the distribution functions. Thanks to the use of an advanced regularised collision operator [22], the coupling boundary condition is found to be directly included in the LB scheme thus requiring no additional computations or storage. Furthermore, a coupling between the LBM and other time advance schemes is introduced and thoroughly discussed in order to preserve the flexibility of the time-integration offered by the use of NS solvers.

The paper is organised as follows. In Section 2, the numerical methods adopted for the present study, namely the Navier-Stokes finite-volume (NS-FV) solver and the lattice Boltzmann method with HRR col-

lision operator, are presented. Then, the coupling procedure between both solvers is described in Section 3 which covers: (1) the rescaling of flow quantities, (2) a specific thermodynamic closure, (3) the reconstruction of distribution functions, and (4) the coupling of time-marching schemes. In Section 4, numerical validations are performed on academic test cases. The capabilities of the hybrid lattice Boltzmann - Navier-Stokes method are finally fully demonstrated on the aeroacoustic study of the flow past a circular cylinder on a hybrid curvilinear-Cartesian grid. This last test case will highlight the ability of the present hybrid method to perform simultaneously wall- and acoustically-resolved simulations in a competitive CPU time.

2. Numerical methods

In this section, the numerical methods used in the framework of the lattice Boltzmann - Navier-Stokes coupling are briefly introduced. All the methods presented hereafter are part of the FAST (Flexible Aerodynamic Software Technology) CFD suite developed at ONERA [23] which consists of Python modules implementing High Performance Computing (HPC) dedicated solvers for unsteady fluid dynamics applications. In addition, all the pre- and post-processing tasks were performed using Cassiopee [24].

2.1. The finite-volume Navier-Stokes flow solver

The three-dimensionnal compressible unsteady Navier-Stokes (NS) equations are solved using ONERA's FastS solver dedicated to multi-block structered grids. Starting from the the conservative form of the Navier-Stokes equations:

$$\frac{\partial}{\partial t}\mathbf{U} + \boldsymbol{\nabla}\cdot\mathbf{F}(\mathbf{U}) - \boldsymbol{\nabla}\cdot\mathbf{F}^{\nu}(\mathbf{U}) = \mathbf{0}, \tag{1}$$

where $\mathbf{U} = (\rho, \rho u_i, \rho E)^t$, $\mathbf{F}(\mathbf{U})$ and $\mathbf{F}^{\nu}(\mathbf{U})$ are the flow variable vectors, the inviscid and viscous fluxes, respectively; the cell-centered finite volume method is obtained by splitting the computational domain Ω into N non-overlapping cells Ω_{ijk}. The integration of equation (1) over every cell of the mesh leads to a semi-discrete form as:

$$\frac{\mathrm{d}}{\mathrm{d}t}\mathbf{U}_{ijk} + \frac{1}{|\Omega_{ijk}|}\mathbf{R}_{ijk}(\mathbf{U}) = \mathbf{0}, \tag{2}$$

where $\mathbf{U}_{ijk}$ is now the mean flow variable vector evaluated at the center of Ω_{ijk}, $|\Omega_{ijk}|$ the volume of Ω_{ijk} and $\mathbf{R}_{ijk}$ the residual of the discretised convective and viscous terms. Actually, the residual is defined as the algebraic sum of the convective and viscous fluxes over the whole boundary of a cell.

The convective fluxes are being approximated with a second-order accurate scheme proposed by Mary & Sagaut [25]. It relies on a hybrid centered/decentered modification of the AUSM+(P) scheme (see Edwards & Liou [26]) offering a good trade-off between robustness, accuracy, and computational cost. The viscous fluxes are discretised by a second-order accurate centered scheme. The time integration can be carried out by means of an explicit 3^{rd}-order accurate low-storage Runge-Kutta scheme [27] or by means of the implicit 2^{nd}-order accurate backward scheme of Gear with local Newton sub-iterations [28]. In the case of the implicit

time-stepping scheme, the Jacobians are approximated following the procedure presented in [29, 30] and the linear system is solved by the LU-SGS factorisation [29].

FastS solver has been extensively used and validated for both academic and industrial unsteady flow simulations such as transitional separation bubble [31], airfoils in near stall configurations [25, 32] and laminar transonic buffet [33]. One major feature of this solver is its computational efficiency since it enables to update over one complete time step up to 3.5 million cells per second and per core on a single Intel Broadwell processor [34].

2.2. The lattice Boltzmann method

2.2.1. Basics of the lattice Boltzmann method

Unlike the finite-volume method described in Section 2.1, the lattice Boltzmann method [4, 5, 6] does not directly rely on the resolution of the Navier-Stokes equations. In fact, it originates from a very specific discretisation of the Boltzmann equation describing the evolution of gases in terms of distribution functions $f(\boldsymbol{x}, \boldsymbol{\xi}, t)$. These can be viewed as representing the probability density of finding fictive particles at a location $\boldsymbol{x}$ and time t being advected at a given velocity $\boldsymbol{\xi}$. In the absence of a body-force term, the Boltzmann equation is given by:

$$\frac{\partial}{\partial t} f(\boldsymbol{x}, \boldsymbol{\xi}, t) + \boldsymbol{\xi} \cdot \frac{\partial}{\partial \boldsymbol{x}} f(\boldsymbol{x}, \boldsymbol{\xi}, t) = -\frac{1}{\tau} \left(f - f^{eq} \right), \tag{3}$$

where the BGK collision operator [35] has been used to model the time evolution of the distribution functions due to collisions between particles. The main idea behind the BGK model is to describe the collisions only through their average effect which can be viewed as a relaxation process towards a local equilibrium f^{eq} with a single relaxation time τ.

In order to solve (3), one should not only discretise space and time like in standard NS solvers, but also the velocity space. This step is of utmost importance and gives the LBM its originality. The main idea is to restrict the continuous velocity space to a finite set of q velocities $\{\boldsymbol{\xi}_i\}_{i \in [\![1;q]\!]}$ so that the macroscopic behavior of the Navier-Stokes equations is still recovered. To perform this discretisation, a standard Gauss-Hermite quadrature is commonly employed [36, 37]. As a result, the Boltzmann equation is now solved for a discrete set of distribution functions $\{f_i\}_{i \in [\![1;q]\!]}$ where f_i is associated with the discrete velocity $\boldsymbol{\xi}_i$. The resulting equation is called the discrete velocity Boltzmann equation (DVBE) and reads:

$$\frac{\partial}{\partial t} f_i(\boldsymbol{x}, t) + \boldsymbol{\xi}_i \cdot \frac{\partial}{\partial \boldsymbol{x}} f_i(\boldsymbol{x}, t) = -\frac{1}{\tau} \left(f_i - f_i^{eq} \right) \qquad i \in [\![1 \ ; \ q]\!]. \tag{4}$$

The set of discrete velocities $\{\boldsymbol{\xi}_i\}_{i \in [\![1;q]\!]}$ is often referred to as a DdQq lattice, where d is the spatial dimension and q the number of discrete velocities. For this study, the usual D3Q19 lattice represented on Figure 1 is used. It is defined by a set of 19 discrete velocities $\boldsymbol{\xi_i}$, their associated Gaussian weights w_i, and by a lattice constant c_s corresponding to the lattice speed of sound.

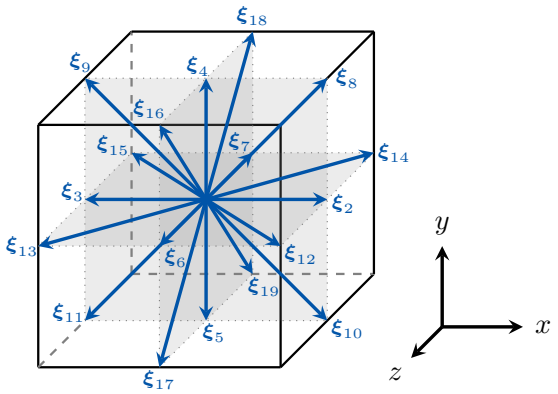

$$c_s = \frac{1}{\sqrt{3}}$$

i	1	$[\![2;7]\!]$	$[\![8;19]\!]$
$\boldsymbol{\xi}_i$	(0,0,0)	$(\pm1,0,0)$ $(0,\pm1,0)$ $(0,0,\pm1)$	$(\pm1,\pm1,0)$ $(\pm1,0,\pm1)$ $(0,\pm1,\pm1)$
w_i	1/3	1/18	1/36

Figure 1: D3Q19 velocity set. The cube, drawn in solid lines, has an edge length of $2\Delta x$. For the sake of clarity, the rest velocity $\boldsymbol{\xi}_1 = \mathbf{0}$ is not represented as it lies at the center of the cube. Each discrete velocity $\boldsymbol{\xi_i}$ is expressed in its non-dimensional form.

The macroscopic quantities of interest for an athermal flow such as the density ρ and the velocity field $\boldsymbol{u}$ can be deduced from the set of discrete distribution functions by taking their moments:

$$\rho(\boldsymbol{x},t) = \sum_{i=1}^{q} f_i(\boldsymbol{x},t) = \sum_{i=1}^{q} f_i^{eq}(\boldsymbol{x},t) \qquad \rho\boldsymbol{u}(\boldsymbol{x},t) = \sum_{i=1}^{q} \boldsymbol{\xi}_i f_i(\boldsymbol{x},t) = \sum_{i=1}^{q} \boldsymbol{\xi}_i f_i^{eq}(\boldsymbol{x},t). \tag{5}$$

Nevertheless, restricting the velocity space to only 19 discrete velocities has an impact on the macroscopic equations recovered by the DVBE and consequently by the LBM. As shown in [37] this gives rise to an athermal flow hypothesis (i.e. $T = T_0$ leading to a speed of sound $c_0^{ath} = \sqrt{RT_0}$ with R the specific gas constant) as well as a cubic Mach error term in the momentum equations [4, 38] thereby limiting the application of standard lattice Boltzmann methods to weakly compressible and low-mach number flows.

In order to obtain the well-known LBM "Stream & Collide" algorithm, the space and time discretisation of the DVBE (4) has to be performed. Thanks to its mathematical structure, the left-hand side (LHS) linear convection term of Equation (4) is integrated along the $\boldsymbol{\xi}_i$ characteristic ensuring an exact advection step and a direct link between the grid and time step through $\Delta x = |\boldsymbol{\xi}_i|\Delta t$. On the other hand, a trapezoidal integration rule is employed for the right-hand side (RHS) collision term. This strategy, leads to a system of two equations :

$$\begin{cases} g_i(\boldsymbol{x} + \boldsymbol{\xi}_i\Delta t, t + \Delta t) &= g_i^{coll}(\boldsymbol{x},t), \\ g_i^{coll}(\boldsymbol{x},t) &= g_i(\boldsymbol{x},t) - \dfrac{\Delta t}{\overline{\tau}}\left(g_i(\boldsymbol{x},t) - g_i^{eq}(\boldsymbol{x},t)\right), \end{cases} \tag{6}$$

where $\overline{\tau} = \tau + \frac{\Delta t}{2}$ and $\{g_i\}_{i\in[\![1;q]\!]}$ are the modified distribution functions so as to ensure an explicit formulation of the algorithm [39]. They are related to the original distribution functions $f_i(\boldsymbol{x},t)$ through the relation

$$g_i(\boldsymbol{x},t) = f_i(\boldsymbol{x},t) + \frac{\Delta t}{2\tau}(f_i(\boldsymbol{x},t) - f_i^{eq}(\boldsymbol{x},t)), \tag{7}$$

which implies $g_i^{eq}(\boldsymbol{x},t) = f_i^{eq}(\boldsymbol{x},t)$. In Equation (6), the *coll* superscript refers to the post-collision state.

The lattice Boltzmann method is classically applied in a non-dimensional form. Therefore, the time-step Δt (resp. the grid-step Δx) is chosen as the characteristic time (resp. characteristic length) for the non-dimensionalization. This leads to the lattice Boltzmann scheme:

$$g_i(\boldsymbol{x} + \boldsymbol{\xi}_i, t+1) = g_i(\boldsymbol{x}, t) - \frac{\Delta t}{\overline{\tau}} \left(g_i(\boldsymbol{x}, t) - g_i^{eq}(\boldsymbol{x}, t) \right). \tag{8}$$

An important point when focusing on acoustics is the physical speed of sound simulated by the LBM denoted hereafter by c_0^{LBM}. Indeed, the athermal sound speed $c_0^{ath} = \sqrt{RT_0}$ imposed by the D3Q19 lattice does not correspond to the expected one $c_0 = \sqrt{\gamma RT_0}$ where γ is the heat capacity ratio. However, in practice, one can enforce $c_0^{\mathrm{LBM}} = c_0$ by computing the time-step following the acoustic scaling. The physical values of the speed of sound c_0^{LBM} and the viscosity ν are then given by:

$$c_0^{\mathrm{LBM}} = c_0 = \frac{c_s \Delta x}{\Delta t} \quad \text{and} \quad \nu = (c_0^{\mathrm{LBM}})^2 \left(\overline{\tau} - \frac{1}{2} \right), \tag{9}$$

where $c_s = 1/\sqrt{3}$ is the D3Q19 lattice constant. Note that the acoustic scaling is equivalent to setting the LBM fictitious temperature to γT_0 where γ is the heat capacity ratio of the fluid to be simulated.

Based on these parameters, the LBM recovers the athermal and low-compressible Navier-Stokes dynamics with a second-order accuracy in both space and time [4, 40].

2.2.2. The Hybrid Recursive Regularised collision operator

The basic lattice Boltzmann method with the single relaxation time BGK collision model presented in Section 2.2.1 suffers from stability issues especially in the low viscosity regime (i.e. at high Reynolds number) [41]. These issues have been attributed to interactions between so called "non-hydrodynamic" modes arising from the space and time discretisation of Equation (4) [42, 43, 44]. To alleviate this problem, a great number of collision models have been proposed such as Multiple Relaxation Times (MRT) operators [41, 45, 46], entropic LBMs [47], and regularised approaches [48, 49]. Some authors also suggest to employ selective filters [50, 51] in order to remove the high wave number instabilities without affecting the large scale dynamics. The present work focuses on the former regularisation strategy as it can easily be linked to the coupling methodology as will be seen in Section 3.4.

The Hybrid Recursive Regularised (HRR) collision operator [22] will be employed hereafter. Following the idea of Latt and Chopard [48], before the collision step, distribution functions are regularised as:

$$g_i^{reg} = g_i^{eq} + g_i^{(1),reg}, \tag{10}$$

where $g_i^{eq} = f_i^{eq}$ is the equilibrium distribution function and $g_i^{(1),reg}$ the regularised contribution based on the 1^{st}-order off-equilibrium term of the Chapmann-Enskog analysis. The lattice Boltzmann scheme with HRR collision operator reads:

$$g_i(\boldsymbol{x} + \boldsymbol{\xi}_i, t+1) = g_i^{eq}(\boldsymbol{x}, t) + \left(1 - \frac{1}{\overline{\tau}} \right) g_i^{(1),reg}(\boldsymbol{x}, t) + \frac{1}{2} \psi_i(\boldsymbol{x}, t). \tag{11}$$

In Equation (11), a corrective term denoted by ψ_i is introduced following [52]. Although this term was initially intended to correct the cubic error of the LBM with a D3Q19 lattice, it was shown recently that the ψ_i corrective term is mandatory to ensure the stability of the HRR model in the low-viscosity regime [53]. This correction reads:

$$\psi_i = -w_i \frac{\mathcal{H}^{(2)}_{i,\alpha\beta}}{2c_s^4} \frac{\partial \Psi_{\alpha\beta\gamma}}{\partial x_\gamma} \tag{12}$$

where $\mathcal{H}^{(2)}_{i,\alpha\beta} = \xi_\alpha \xi_\beta - c_s^2 \delta_{\alpha\beta}$ is the second-order discrete Hermite polynomial, and $\Psi_{\alpha\beta\gamma}$ is the deviation term between of the third-order moment of the velocity-discrete equilibrium and its continuous counterpart. In the present study, the derivatives are estimated with a second-order centered finite-difference scheme. The reader is referred to [52] for an in-depth discussion of this corrective term.

In the same way as for the recursive regularised collision model of Malaspinas [49], both the equilibrium and the regularised off-equilibrium distribution functions are expanded using the Hermite formalism:

$$g_i^{eq} = w_i \sum_{n=0}^{N} \frac{1}{c_s^{2n} n!} \boldsymbol{a}_0^{(n)} : \boldsymbol{\mathcal{H}}_i^{(n)} \quad \text{and} \quad g_i^{(1),reg} = w_i \sum_{n=2}^{N_r} \frac{1}{c_s^{2n} n!} \boldsymbol{a}_1^{(n)} : \boldsymbol{\mathcal{H}}_i^{(n)}, \tag{13}$$

where ":" stands for the full contraction of indices of two n^{th}-order tensors: the Hermite coefficients $\boldsymbol{a}_0^{(n)}$ and $\boldsymbol{a}_1^{(n)}$, and the discrete Hermite polynomials $\boldsymbol{\mathcal{H}}_i^{(n)} = \boldsymbol{\mathcal{H}}^{(n)}(\boldsymbol{\xi}_i)$. In the present work, $N = N_r = 3$. It is also worth noting that, as introduced in [22], judicious combinations of third-order Hermite polynomials are used to built the third-order contributions in g_i^{eq} and $g_i^{(1),reg}$, leading to:

$$\begin{aligned}
\boldsymbol{a}_\alpha^{(3)} : \boldsymbol{\mathcal{H}}_i^{(3)} = {} & 3\left(\mathcal{H}^{(3)}_{i,xxy} + \mathcal{H}^{(3)}_{i,yzz}\right)\left(a^{(3)}_{\alpha,xxy} + a^{(3)}_{\alpha,yzz}\right) + \left(\mathcal{H}^{(3)}_{i,xxy} - \mathcal{H}^{(3)}_{i,yzz}\right)\left(a^{(3)}_{\alpha,xxy} - a^{(3)}_{\alpha,yzz}\right) \\
& + 3\left(\mathcal{H}^{(3)}_{i,xzz} + \mathcal{H}^{(3)}_{i,xyy}\right)\left(a^{(3)}_{\alpha,xzz} + a^{(3)}_{\alpha,xyy}\right) + \left(\mathcal{H}^{(3)}_{i,xzz} - \mathcal{H}^{(3)}_{i,xyy}\right)\left(a^{(3)}_{\alpha,xzz} - a^{(3)}_{\alpha,xyy}\right) \\
& + 3\left(\mathcal{H}^{(3)}_{i,yyz} + \mathcal{H}^{(3)}_{i,xxz}\right)\left(a^{(3)}_{\alpha,yyz} + a^{(3)}_{\alpha,xxz}\right) + \left(\mathcal{H}^{(3)}_{i,yyz} - \mathcal{H}^{(3)}_{i,xxz}\right)\left(a^{(3)}_{\alpha,yyz} - a^{(3)}_{\alpha,xxz}\right),
\end{aligned} \tag{14}$$

for $\alpha = 0$ and 1. By definition, the Hermite polynomials $\mathcal{H}^{(3)}_{i,\gamma\gamma\delta}$ are given by $\mathcal{H}^{(3)}_{i,\gamma\gamma\delta} = \xi^2_{i\gamma}\xi_{i\delta} - c_s^2 \xi_{i\delta}$. The formulas of the equilibrium and off-equilibrium Hermite coefficients are provided in Table 1.

	$n=0$	$n=1$	$n=2$	$n=3$
$\boldsymbol{a}_0^{(n)}$	$a_0^{(0)} = \rho$	$a^{(1)}_{0,\alpha} = \rho u_\alpha$	$a^{(2)}_{0,\alpha\beta} = \rho u_\alpha u_\beta$	$a^{(3)}_{0,\alpha\beta\gamma} = \rho u_\alpha u_\beta u_\gamma$
$\boldsymbol{a}_1^{(n)}$	$a_1^{(0)} = 0$	$\boldsymbol{a}_1^{(1)} = \boldsymbol{0}$	Equation (15)	$a^{(3)}_{1,\alpha\beta\gamma} = u_\alpha a^{(2)}_{1,\beta\gamma} + u_\beta a^{(2)}_{1,\alpha\gamma} + u_\gamma a^{(2)}_{1,\alpha\beta}$

Table 1: Formulas of the equilibrium and off-equilibrium Hermite coefficients. All these expressions, except the one for $\boldsymbol{a}_1^{(2)}$, were derived using Malaspinas' recursive formulas [49].

The very essence of the HRR collision operator lies in the way the second-order off-equilibrium Hermite coefficient $\boldsymbol{a}_1^{(2)}$ is computed [22]. In the HRR framework, this tensor is hybridised. It is decomposed into a

linear combination of a projected regularised part and a finite difference part, yielding:

$$\boldsymbol{a}_1^{(2)} = \sigma \left[\sum_{i=1}^{q} \boldsymbol{\mathcal{H}}_i^{(2)} \left(g_i - g_i^{eq} + \frac{\psi_i}{2} \right) \right] + (1-\sigma) \left[-\rho \overline{\tau} c_s^2 \left(\boldsymbol{\nabla u} + (\boldsymbol{\nabla u})^t \right) \right] \quad \text{with } 0 \leq \sigma \leq 1. \tag{15}$$

The spatial derivatives of the velocity field present in Equation (15) are evaluated with second-order centered finite differences. σ is a user-tuned parameter to control the amount of hyper-viscosity added to the model [22]. In the remainder of this paper the value $\sigma = 0.995$ is adopted since numerical tests have indicated that this specific value of σ allows to obtain stable computations while limiting the numerical dissipation of shear and acoustic waves to a very small extent.

3. Lattice Boltzmann - Navier-Stokes coupling

Having presented the main components of the lattice Boltzmann and finite-volume solvers used for this study, the focus is now made on the coupling between both methods. First, some general notions about the coupling interface are introduced. This will help to highlight the main issues to resolve before setting up a coupled simulation. As a result of this discussion, the rescaling step, the thermodynamic closure as well as the reconstruction of the distribution functions and the temporal coupling are introduced and discussed.

3.1. The coupling interface

To illustrate the basic idea of the lattice Boltzmann - Navier-Stokes coupling, a simplified one-dimensional case represented on Figure 2 is studied. The computational domain denoted by Ω is decomposed into two sub-domains Ω_{NS} and Ω_{LBM} such that $\Omega = \Omega_{\text{NS}} \cup \Omega_{\text{LBM}}$ and $\Omega_{\text{NS}} \cap \Omega_{\text{LBM}} = \varnothing$. The finite volume method is applied in Ω_{NS} and the lattice Boltzmann method is applied in Ω_{LBM}. In the following, both solvers are supposed to be cell-centered as it the case for ONERA's FAST CFD suite. Moreover, it is also assumed that both domains have the same grid size Δx at least in the vicinity of the interface. The following methodology can then be extended with few changes to any more general boundary. Indeed, when the cells centers do not coincide at the interface, spatial interpolation has to be added to the following procedure.

The finite volume scheme is applied on the Navier-Stokes Finite-Volume (NS-FV) interior cells (○). To be consistent with the finite volume solver presented in Section 2.1 which is based on a five-point stencil, two layers of ghost cells are required at the borders of the Ω_{NS} sub-domain to specify the coupling boundary condition. The information transfer from the LBM domain to the NS domain (⟶) then consists in imposing the flow variable vector $\mathbf{W} = (\rho, u_i, T)^t$ at the NS-FV boundary nodes (○). With the help of Equation (5), the first macroscopic variables of $\mathbf{W}$ are easily obtained by taking the discrete moments of the distribution functions in the corresponding LBM donor cells (□). However, some attention has to be paid to the fact that the LBM solver has its own system of "lattice units" in contrast to the NS-FV solver. Moreover, as evidenced in Section 2.2.1, the use of a D3Q19 lattice imposes a constant temperature $T = T_0$ and a

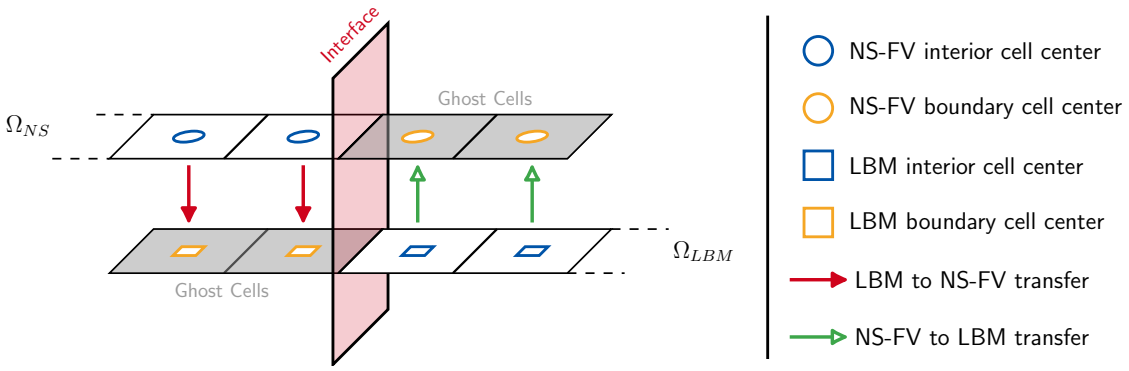

Figure 2: One dimensional representation of a coupling interface. The computational domain is decomposed into a finite-volume Navier-Stokes sub-domain Ω_{NS} and a LB sub-domain Ω_{LBM}. No overlapping region where both methods are simultaneously applied is needed. The information exchange is only ensured through the ghost-cells.

barotropic equation of state which does not coincide with the perfect gas law simulated by the finite-volume method. As a consequence, a rescaling step and a temperature closure are needed to fully determine the LBM to NS-FV transfer ( ). This will be the topic of Sections 3.2 and 3.3.

Symetrically, the lattice Boltzmann "Stream & Collide" algorithm is applied on the LBM interior cells ( ) while the ghost cells ( ) are used to specify the coupling boundary condition. Here again, two layers of ghost cells are defined. The information transfer from the NS domain to the LBM domain ( ) is not as straightforward as the inverse owing to the fact that the information provided by the donor cells ( ) of the FV solver (i.e. the 5 components of the flow variable vector $\mathbf{W} = (\rho, u_i, T)^t$) only represents a subset of the information needed on the scale of the distribution functions (i.e the 19 distribution functions for a D3Q19 lattice). Hence, a one-to-many problem arises. Therefore, it is of utmost importance to understand how to link the macroscopic variables to the LB set of distribution functions. This specific issue is at the heart of the coupling procedure and will be addressed in Section 3.4.

To end this discussion on the simplified case of Figure 2, a remark has to be made regarding the time advance procedure in the presence of a coupling interface. By construction, the LBM is an explicit scheme with constant CFL number, unlike the finite volume method which offers various time-stepping options. As a consequence, it might be very likely that the two schemes do not use the same time stepping strategy. In Section 3.5, a methodology to bridge the LBM with other time advance schemes is proposed.

3.2. Rescaling of macroscopic flow quantities

At the coupling interface between the lattice Boltzmann and the Navier-Stokes solver, only macroscopic quantities (i.e. the 5 components of the flow state vector $\mathbf{W} = (\rho, u_i, T)^t$) will be exchanged between the solvers inasmuch as they are the only variables in common to both numerical methods. If the cells centers coincide at the interface, it is sufficient to copy the values from one grid to the other, but if not, an

interpolation step is required in order to evaluate the variables at the centers of the receiving grid. Now, regardless of the transfer type, a rescaling step has to be performed for each exchange since the lattice Boltzmann and Navier-Stokes solvers are implemented in different systems of units. Hereafter, any variable v expressed in lattice units will be denoted by $\tilde{v}$ while $\overline{v}$ refers to its Navier-Stokes non-dimensional value.

As stated in Section 2.2, the lattice Boltzmann method is expressed in a very specific set of units often referred to as the "lattice units" where the grid- and time-step Δx and Δt are used as characteristic length and time scales for the non-dimensionalization. The density field is also made non-dimensional so that, in average, $\tilde{\rho}^{\mathrm{LBM}} = \rho^{\mathrm{LBM}}/\rho_0 = 1$ where ρ_0 is the density scaling factor. In the same way, it is of common practice to use dimensionless quantities for a finite-volume Navier-Stokes solver. However it should be noted that the conversion factors in the NS framework are most of the time chosen as flow dependent quantities (the free-stream velocity U_∞, density ρ_∞, and a geometrical characteristic length L_0 for instance) rather than numerical parameters such as Δx and Δt. Consequently when exchanging data between the LB and NS-FV solvers, the following scaling formulas have to be applied:

$$\overline{\rho}^{\mathrm{NS}} = \frac{\rho_0 \tilde{\rho}^{\mathrm{LBM}}}{\rho_\infty} = \frac{\rho_0}{\rho_\infty} \sum_{i=1}^{q} g_i(\boldsymbol{x}, t) \quad \text{and} \quad \overline{u}_i^{\mathrm{NS}} = \frac{\tilde{u_i}^{\mathrm{LBM}} \dfrac{\Delta x}{\Delta t}}{U_\infty} = \frac{\Delta x}{U_\infty \Delta t \tilde{\rho}^{\mathrm{LBM}}} \sum_{j=1}^{q} \boldsymbol{\xi}_i g_j(\boldsymbol{x}, t). \tag{16}$$

In Equation (16), Δt and Δx refer to the time- and grid-steps of the donor solver. Obviously, the case of a dimensional NS-FV solver is directly obtained by setting $U_\infty = \rho_\infty = 1$.

The last variable which has to be provided to the NS-FV solver, is the temperature. However, as already stated, the D3Q19 lattice employed by the LB solver only solves an athermal version of the Navier-Stokes equations and thus imposes a constant temperature $T = T_0$. In order to alleviate this issue, some work on the thermodynamic closure has to be done.

3.3. Thermodynamic closure

All the previous work done on coupled LB-NS simulations relied on an incompressible Navier-Stokes flow solver [13, 15, 20, 21]. Consequently, only the velocity field had to be provided to the NS solver while the pressure field was computed via the embedded Poisson solver. Conversely, the density field which is needed for the LBM was directly computed from the NS pressure field. Extending this methodology to a compressible Navier-Stokes solver is not as straightforward.

The present methodology suggests to use pressure as an intermediate variable to compute temperature fluctuations around its reference value T_0. The virtual fluid simulated by the standard lattice Boltzmann method relies on a barotropic equation of state which reads as:

$$p^{\mathrm{LBM}} = \rho (c_0^{\mathrm{LBM}})^2 = \rho_0 (c_0^{\mathrm{LBM}})^2 + \rho' (c_0^{\mathrm{LBM}})^2 = p_0^{\mathrm{LBM}} + \rho' (c_0^{\mathrm{LBM}})^2, \tag{17}$$

where the density has been decomposed as $\rho = \rho_0 + \rho'$ (ρ_0 being the reference density and ρ' its fluctuating part) and where $c_0^{\mathrm{LBM}} = \sqrt{\gamma R T_0}$ is the lattice Boltzmann speed of sound owing to the acoustic scaling. Even though this equation of state does not correspond to any physical fluid, it can be linked to more general equations of state. Indeed, for small and nearly-isentropic disturbances any equation of state $p = p(\rho, s)$ can be linearised as [54]:

$$p = p_0 + p' \approx p_0 + \rho' \left(\frac{\partial p}{\partial \rho} \right)_s = p_0 + \rho' c_0^2, \tag{18}$$

where $p_0 = \rho_0 R T_0$ and ρ_0 are the reference pressure and density, p' and ρ' the pressure and density deviations w.r.t their reference value, and $c_0 = \sqrt{\gamma R T_0}$ the physical speed of sound. By comparing the fluctuating parts of Equations (17) and (18), it can be seen that the LBM correctly computes the pressure fluctuations even though the LBM reference pressure p_0^{LBM} does not correspond to the one in Equation (18) (they differ by a factor of γ). Therefore, starting from the pressure fluctuations calculated by the LBM, it is proposed to reconstruct the temperature fluctuations around its reference value T_0 by using perturbed perfect gas law:

$$T' = \frac{p' - \rho' R T_0}{(\rho_0 + \rho') R} = \frac{\rho' \left[(c_0^{\mathrm{LBM}})^2 - R T_0 \right]}{(\rho_0 + \rho') R}, \tag{19}$$

where R is the specific gas contant. To ensure the validity of the temperature reconstruction $T = T_0 + T'$ where T' is computed thanks to Equation (19), the coupling methodology presented in this paper imposes some restrictions on the location of the interface between both solvers. As a matter of fact, it has to lie in flow regions where the linearised Equation (18) is valid, i.e. in regions where entropy fluctuations are negligible (e.g. in linear acoustics zones). To overcome this limitation, lattice Boltzmann methods including thermal or ideal gas compressibility effects can be implemented (for instance by using multispeed lattices [55], double distribution functions [56] or by coupling an extra energy equation, solved by finite differences, to the LBM [57]). This will be the subject of future work.

3.4. Reconstruction of the distribution functions

With the results of Sections 3.2 and 3.3, a direct mapping from the distribution functions to the flow state variables has been established. However, the spatial coupling introduced in this paper requires a two-way exchange. Therefore, it is crucial to understand how the LB set of distribution functions can be derived from the macroscopic flow state vector $\mathbf{W} = (\rho, u_i, T)^t$. Given its mesoscopic nature, the LBM genuinly gathers more information than at the continuum level. Indeed, with the D3Q19 lattice, $q = 19$ distribution functions have to be specified at the coupling interface arising from $D + 2 = 5$ flow variables computed by the NS-FV solver. As a consequence, a one-to-many problem occurs. The same problem also appears when initialising a LBM computation from macroscopic data [58].

Following the idea of Skordos [58], the vast majority of hybrid lattice Boltzmann - Navier-Stokes methods propose to split the distribution functions into an equilibrium and an off-equilibrium part. While the

equilibrium part can be directly computed thanks to its analytical formula, off-equilibrium distribution functions can be determined by several manners. Albuquerque *et al.* [14] proposed to express them analytically through a Chapman-Enskog expansion. Such methodology has also been applied in similar ways in [16, 59]. On the other side, Neumann *et al.* [19] solved a constrained-optimisation problem by ensuring the mass, momentum and viscous stresses conservation at the interface in order to obtain the corresponding off-equilibrium distribution functions. It should be noted that other methods using completely different approaches were also developed such as constrained runs [59], velocity-boundary coupling [60] or statistical inference [61].

The distribution functions reconstruction methodology proposed in this paper follows the fundamental idea of Albuquerque *et al.* [14] relying on a Chapman-Enskog expansion and further extends it without any prior assumption on the distribution functions. The hybrid method being designed for unsteady aerodynamic and aeroacoustic application, solving an optimisation problem on each interface cell at each time step seems, at first glance, quite expensive in terms of CPU time. Consequently, in the ghost cells of the LB solver, the distribution functions will be given by (see Figure 2 for notations):

$$g_i(\square, t) = g_i^{eq}(\mathbf{U}(\bigcirc, t)) + g_i^{neq}(\mathbf{U}(\bigcirc, t)) \quad \text{for each} \quad i \in [\![1;\ 19]\!], \tag{20}$$

where the off-equilibrium component g_i^{neq} has to be determined. This is the topic of the present section where a general methodology which can be applied to bridge the LBM with any other macroscopic model is introduced.

3.4.1. Mixed Taylor/Chapman-Enskog expansion

As a first step towards the determination of the off-equilibrium component g_i^{neq}, a mixed Taylor/Chapman-Enskog expansion is performed on the lattice Boltzmann scheme with the corrected HRR collision operator (11) (see Appendix A for the detailed analysis). In all the previous work on hybrid lattice Boltzmann - Navier-Stokes solvers [13, 14, 16, 18], this analysis was conducted by directly expanding the discrete distribution functions g_i around their equilibrium. However, as discussed in [62], there is a difference of one order of magnitude in the expansion parameter between the continuous (f_i) and discrete (g_i) distribution functions. As a consequence, in the analysis reported in Appendix A care has been taken to re-express the discrete distributions (g_i) as a function of the continuous ones (f_i). The following relation is then obtained:

$$\left(\left[\frac{\partial}{\partial t_1} + \boldsymbol{\xi}_i \frac{\partial}{\partial \boldsymbol{x}_1} \right] f_i^{eq} - \psi_i \right) = -\frac{1}{\tau} f_i^{neq,(1)} + \mathcal{O}(\Delta t^2). \tag{21}$$

This equation is the cornerstone of the coupling procedure. Indeed, it shows that the first-order truncated off-equilibrium distribution functions $f_i^{neq,(1)}$ are completely determined by the knowledge of the equilibrium distribution function and its associated space- and time-derivatives. Moreover, the first-order approximation

of f_i^{neq} has been shown to be sufficient to recover the macroscopic Navier–Stokes equations [37]. Therefore, the off-equilibrium contribution which has to be considered when reconstructing the distributions in the ghost cells of the LB solver is restricted to $f_i^{neq,(1)}$.

As highlighted by the $\mathcal{O}(\Delta t^2)$ error-term in Equation (21), the defining relation of $f_i^{neq,(1)}$ is second-order accurate which means that the second-order convergence of the LB scheme is naturally preserved.

3.4.2. Expressing the off-equilibrium contribution

Equation (21) clearly shows that the first-order approximation of the off-equilibrium distribution functions $f_i^{neq,(1)}$ is directly linked to gradients of the equilibrium distribution function f_i^{eq}. Yet, f_i^{eq} depends only on the macroscopic fields $\rho(\boldsymbol{x},t)$ and $\rho\boldsymbol{u}(x,t)$, thus it becomes clear that $f_i^{neq,(1)}$ will likewise depend on the macroscopic fields and also on their gradients. This last point is of utmost importance as it brings in new information at the coupling interface and thus helps alleviating the one-to-many problem when reconstructing the distribution functions from the macroscopic variables. Having said that, the analytical expression of $f_i^{neq,(1)}$ as a function of the macroscopic variables still has to be determined. In the present methodology, no prior approximations are made on the distribution functions f_i unlike in [13] where second-order terms in the equilibrium and both temporal and spatial derivatives of $f_i^{neq,(1)}$ were neglected.

The first step is to consider the equilibrium distribution function. Once the equilibrium is chosen, it can directly be replaced in Equation (21). Its time derivative, can then be simplified with the chain rule. As a consequence, time derivatives of macroscopic variables appear through:

$$\frac{\partial f_i^{eq}}{\partial t_1} = \frac{\partial f_i^{eq}}{\partial \rho}\frac{\partial \rho}{\partial t_1} + \frac{\partial f_i^{eq}}{\partial u_k}\frac{\partial u_k}{\partial t_1}, \tag{22}$$

which can also be expressed as spatial derivatives thanks to the macroscopic conservation equations. An analytical formulation of $f_i^{neq,(1)}$ is thereby obtained. Such procedure can be used for any equilibrium distribution function even if they differ from the one proposed in Equation (13).

It will now be shown that when using the hybrid recursive regularised collision operator for the LBM, the analytical expression of $f_i^{neq,(1)}$ is genuinely contained in the scheme. Indeed, in the present study, to ensure a smooth transition between the reconstruction interface and the LBM bulk solver, the same equilibrium as the one of Equation (13) is applied in the ghost cells of the LB solver. The latter relies on a Hermite expansion up to the third order [22]. By projecting Equation (21) onto the basis of Hermite polynomials, it simplifies into (see Appendix B for further details):

$$a^{(n)}_{1,\alpha_1...\alpha_n} = u_{\alpha_n} a^{(n-1)}_{1,\alpha_1...\alpha_{n-1}} + \sum_{i=1}^{n-1} u_{\alpha_1}...u_{\alpha_{n-2}} a^{(2)}_{1,\alpha_i\alpha_n} \quad \text{for } n \geq 3, \tag{23}$$

where $\boldsymbol{a}_1^{(n)}$ if nth-order Hermite coefficient of the off-equilibrium contribution $f_i^{neq,(1)}$, and $\alpha_1, ..., \alpha_n$ are the tensor indices such as $\alpha_i \in \{x, y, z\}$ for each i. Equation (B.4), is almost the same as the one derived in

[49] however a slight difference appears implicitly in the definition of $\boldsymbol{a}_1^{(2)}$ where the corrective term helps to properly remove the $\mathcal{O}(\mathrm{Ma}^3)$ error term which was neglected in [49] (see Appendix B for a short discussion).

In the context of the HRR-LBM and with Equation (B.4), the first-order approximation of the off-equilibrium part of the distribution functions $f_i^{neq,(1)}$ can be expressed as:

$$f_i^{neq,(1)} = w_i \sum_{n=0}^{N} \frac{1}{c_s^{2n} n!} \boldsymbol{a}_1^{(n)} : \boldsymbol{\mathcal{H}}_i^{(n)}, \tag{24}$$

where the Hermite coefficient of the off-equilibrium distributions are given by:

$$\boldsymbol{a}_1^{(0)} = 0, \quad \boldsymbol{a}_1^{(1)} = 0, \quad \boldsymbol{a}_1^{(2)} = -\rho\tau c_s^2 \left(\nabla \boldsymbol{u} + \nabla \boldsymbol{u}^T\right), \quad a_{1,\alpha\beta\gamma}^{(3)} = u_\alpha a_{1,\beta\gamma}^{(2)} + u_\beta a_{1,\alpha\gamma}^{(2)} + u_\gamma a_{1,\alpha\beta}^{(2)}. \tag{25}$$

By comparing Equations (24) and (25) with Equation (13) and Table 1, it becomes clear that the analytical expression of $f_i^{neq,(1)}$ can be interpreted with regard to the one given by the HRR collision operator. Indeed, it is equivalent to applying the regularisation step in the ghost cells with a value of $\sigma = 0$ with the sole difference that all the macroscopic information is provided by the NS-FV solver. It has to be noticed that the choice of $\sigma = 0$ for the reconstruction of the off-equilibrium part introduces some numerical dissipation. However, this value is only applied in the ghost-cells of the LB solver thereby limiting its effect to a very small extent of the computational domain. As will be seen in Section 4, the numerical dissipation induced by $\sigma = 0$ in the ghost cells is found to be unnoticeable.

All in all, the missing distribution functions specified at the NS-FV to LBM interface are reconstructed by using the decomposition $f_i = f_i^{eq} + f_i^{neq,(1)}$ where f_i^{eq} and $f_i^{neq,(1)}$ are defined by Equations (13) and (24). The results obtained here with the space- and time-continuous distribution functions f_i have to be transposed to the discrete distribution functions g_i in order to apply Equation (20) in the LB ghost cells. As already stated in Section 2.2, $g_i^{eq} = f_i^{eq}$ in the framework of regularised collision operators. However, concerning the off-equilibrium part, the following relation have has be applied:

$$g_i^{neq,(1)} = \left(1 + \frac{\Delta t}{2\tau}\right) f_i^{neq,(1)} = \frac{\overline{\tau}}{\tau} f_i^{neq,(1)}, \tag{26}$$

meaning that the relations obtained previously remain valid in the discrete case provided that the continuous relaxation time τ is replaced by its discrete counterpart $\overline{\tau}$. The distribution functions $g_i(\square, t)$ (see Figure 2 for notations) are then fully determined by the macroscopic variables and their gradients which will be computed with standard second-order centered finite differences hereafter.

3.5. Coupling of time advance schemes

Having seen how to spatially couple the LBM with the NS-FV solver, the last point to investigate concerns the coupling of time advance schemes. As already discussed in Section 2.2.1, the "Stream & Collide" algorithm of the LBM relies on a specific time and space discretisation leading to a second-order

explicit scheme. Moreover, the physical CFL number is imposed by the lattice constant c_s. As a consequence, the LB scheme in its classical form offers very little flexibility on the time integration scheme. By contrast, the NS-FV schemes are traditionally obtained through the method of lines meaning that both the spatial and temporal scheme can be chosen separately – provided that stability constraints are respected. Two time integration methods can be distinguished: the explicit and implicit ones. Explicit methods offer most of the time better accuracy and increased HPC capabilities. However, their time step is restricted by some stability criteria. Conversely, implicit methods allow bigger time steps due to their increased stability but at incresed computational cost. For this reason, a coupling between the LBM and both explicit and implicit time schemes will be presented. Hereafter, it is assumed that both solvers use a common time step at least on each side of the coupling interface. The time step will be denoted by $\Delta t = \Delta t^{\mathrm{NS}} = \Delta t^{\mathrm{LBM}}$. Extending this methodology to non-conforming time-steps might be the purpose of future work.

3.5.1. LBM/Explicit coupling: the case of Runge-Kutta schemes

A s-step explicit Runge-Kutta (RK) method allows to compute $\mathbf{U}^{n+1}$ – solution of Equation (1) – at time $t_{n+1} = t_n + \Delta t$ by using $\mathbf{U}^n$ and $s-1$ intermediate values. A s-step explicit Runge-Kutta method is defined as:

$$\left\{ \begin{array}{rcl} t^{n,i} & = & t_n + c_i \Delta t, \\ \mathbf{U}^{n,i} & = & \mathbf{U}^n + \Delta t \sum_{j=1}^{i-1} a_{ij} \mathbf{R}^{n,j}, \\ \mathbf{R}^{n,i} & = & \mathbf{R}(\mathbf{U}^{n,i}), \end{array} \right. \tag{27}$$

where $1 \leq i, j \leq s$. The i-th intermediate time, the i-th intermediate value, and the i-th intermediate evaluation of the residual between t_n and $t_n + \Delta t$ are denoted by $t^{n,i}$, $\mathbf{U}^{n,i}$, and $\mathbf{R}^{n,i}$ respectively. The solution at time t^{n+1} is then given by $\mathbf{U}^{n+1} = \mathbf{U}^n + \Delta t \sum_{i=1}^{s} b_i \mathbf{R}^{n,i}$. The method is fully defined by its families of real coefficients a_{ij}, b_i, and c_i.

The key element to notice when trying to couple an explicit RK method with the LB scheme is that boundary conditions need to be specified for each intermediate time $t^{n,i}$. The solution in the LB domain at these instants does not exist since the evolution from t_n to $t_n + \Delta t$ is direct. Hence, the LB solution has to be interpolated for each intermediate time. To illustrate the time coupling procedure, Figure 3 details one time advance step in the case of the RK-3 scheme introduced in Section 2.1.

The RK-3 algorithm relies on the computation of 2 intermediate values thus, two intermediate LB solutions at $t_n + c_1 \Delta t$ and $t_n + c_2 \Delta t$ have to be interpolated in order to correctly apply the NS-FV 5-point stencil at the interface between both solvers. The interpolation is carried out by means of Lagrange polynomials. Given a set of $k+1$ distinct data points $(t_j, \mathbf{U}^j_{\mathrm{LBM}})$, the k-th order Lagrange interpolating

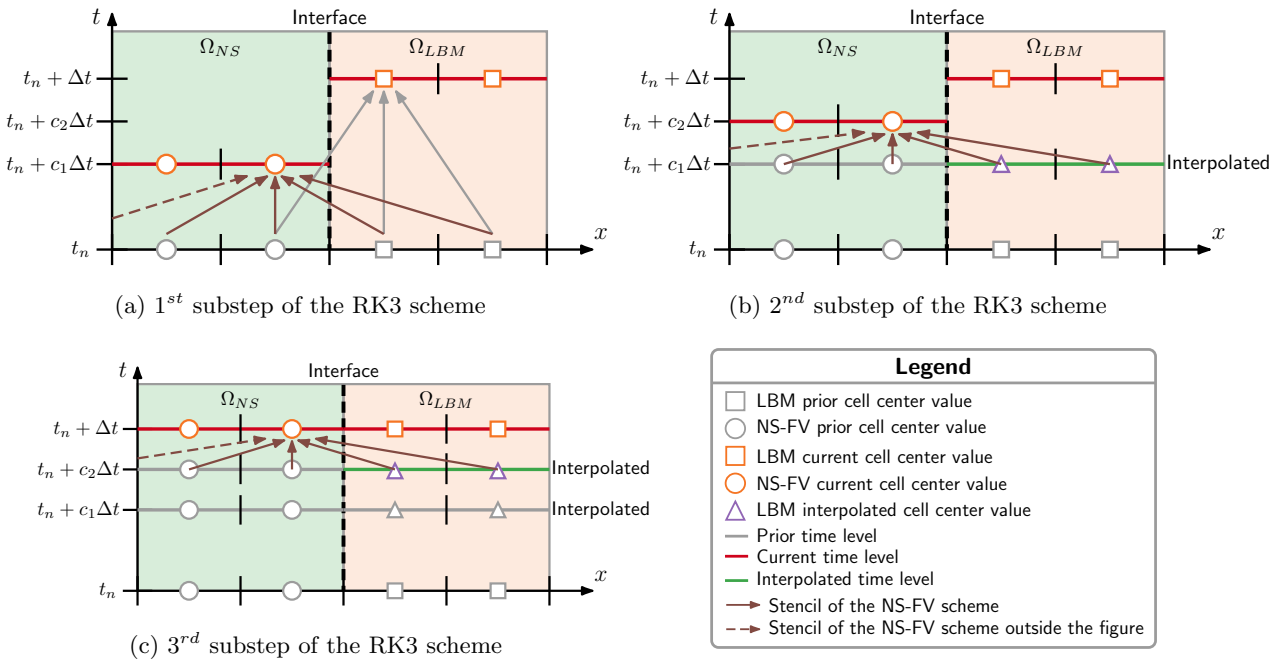

(a) 1^{st} substep of the RK3 scheme

(b) 2^{nd} substep of the RK3 scheme

(c) 3^{rd} substep of the RK3 scheme

Figure 3: Temporal coupling between a 3^{rd} order Runge Kutta scheme (RK3) and the lattice Boltzmann method.

polynomial is a linear combination of Lagrange basis polynomials:

$$\mathcal{L}(t) = \sum_{j=0}^{k} \mathbf{U}_{\text{LBM}}^{j} \left(\prod_{i=0, j\neq i}^{k} \frac{t - t_i}{t_j - t_i} \right). \tag{28}$$

In the following, 0^{th} to 4^{th} order interpolations will be compared. Table 2 summarizes the time levels and solution values used for each interpolation order. The interpolations are computed in a backward manner inasmuch as prior time levels are added to enrich the set of points needed to compute the Lagrange polynomial.

Order	$(t_{n-3}, \mathbf{U}_{\text{LBM}}^{n-3})$	$(t_{n-2}, \mathbf{U}_{\text{LBM}}^{n-2})$	$(t_{n-1}, \mathbf{U}_{\text{LBM}}^{n-1})$	$(t_n, \mathbf{U}_{\text{LBM}}^{n})$	$(t_{n+1}, \mathbf{U}_{\text{LBM}}^{n+1})$
0	❍	❍	❍	❍	✓
1	❍	❍	❍	✓	✓
2	❍	❍	✓	✓	✓
3	❍	✓	✓	✓	✓
4	✓	✓	✓	✓	✓

Table 2: Data points required for the computation of the interpolating Lagrange polynomials. ❍: solution not used, ✓: solution used.

3.5.2. LBM/Implicit coupling: the case of the Gear scheme

In some cases, implicit time stepping might be beneficial due to its ability to deal with larger time steps. To this end, and to take advantage of the flexibility offered to users on choosing between various time-stepping strategies for FV schemes, a coupling procedure between the LBM and an implicit scheme is presented. More particularly, Gear's implicit scheme present in ONERA's FAST CFD suite [28] will be used. Applied to Equation (1), it reads:

$$\boldsymbol{\mathcal{F}}(\mathbf{U}^{n+1}) = 0, \quad \text{where} \quad \boldsymbol{\mathcal{F}}(\mathbf{U}^{n+1}) = \frac{3\mathbf{U}^{n+1} - 4\mathbf{U}^{n} + \mathbf{U}^{n-1}}{2} + \frac{\Delta t}{|\Omega|}\mathbf{R}(\mathbf{U}^{n+1}). \tag{29}$$

The resulting non-linear problem is solved iteratively. At the beginning of each iteration the solution increment is fixed at zero in the NS-FV ghost cells. This corresponds to a Dirichlet condition. Thus, all boundary conditions are treated explicitly in our implementation, which has the advantage of being computationally cheap. The role of the iterations of Newton's internal process is to remove the errors due to the explicit treatment of the boundary conditions. As a result, the coupling of the LB scheme with this implicit time stepping method is straightforward. The LB domains perform their iteration first then, the solution at time t_{n+1} being known, it is applied on the boundaries of every NS domain throughout the entire solving process of Equation (29).

4. Numerical results and hybrid method capabilities

In order to demonstrate the validity of the proposed hybrid lattice Boltzmann - Navier-Stokes method and to highlight its capabilities when computing unsteady flow problems, some aerodynamic and aeroacoustic test cases are conducted. First, the coupling components introduced in Section 3 are discussed on the case of a $1D$ Gaussian acoustic wave. The coupling strategy is then validated with the case of a convected vortex. In addition, the acoustic capabilities of the hybrid method are assessed through the computation of the radiation of a harmonic acoustic source in a fluid medium at rest. Finally, the application of the hybrid lattice Boltzmann - Navier-Stokes method to a representative aeronautical application where both the aerodynamics and acoustics are required is introduced with the study of the flow past a circular cylinder. The computational cost of the proposed hybrid method on this last test case will be discussed and compared to full Navier-Stokes and lattice Boltzmann simulations.

All the simulations of the present study are carried out on pseudo-2D domains with a $10\Delta x$ transverse extension where Δx is the grid step. Thus, the 3D formulation of the Boltzmann and Navier-Stokes lattice solvers is used but periodic boundary conditions are used in the transverse direction so as to ensure that the flow remains perfectly 2D. Moreover, the speed of sound is fixed at $c_0 = 347.3$ m.s^{-1}, the specific gas constant is given by $R = 287.053$ J.kg^{-1}.K^{-1} and the heat capacity ratio is $\gamma = 1.4$.

4.1. Gaussian acoustic plane wave

The first test case introduced here is a convected one dimensional acoustic wave. Besides validating the lattice Boltzmann - Navier-Stokes coupling strategy, this simple problem will also help to highlight the influence of the different coupling components introduced in Section 3.

The computational domain, which is represented in Figure 4, is a periodic box of size $[2L, L, 10\Delta x]$ decomposed in 2 sub-domains Ω_{NS} and Ω_{LBM} of size $[L, L, 10\Delta x]$ each, with L being the reference length equal to 1 m. Periodic boundary conditions are implemented at the borders of the computational domain in the x, y, and z directions. A $1D$ Gaussian acoustic plane wave is initialised at the center of the NS domain and propagates towards the LB domain thus crossing the coupling interface.

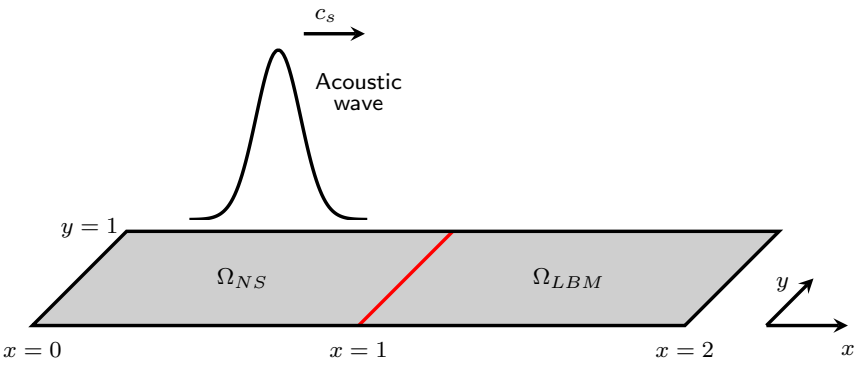

Figure 4: Schematic representation of the $1D$ acoustic plane wave test case.

At the beginning of the computation, the flow variables are defined as follows:

$$\begin{cases} \rho(x) &= \rho_0 \left(1 + A \exp\left(\dfrac{-(x - x_c)^2}{2R_c^2}\right)\right), \\ u_x(x) &= U_x - \dfrac{\rho'}{\rho_0} c_0, \end{cases} \tag{30}$$

where $\rho_0 = 1.1765$ kg.m^{-3} is the free-field density, $A = 10^{-4}$ is the amplitude of the density perturbation, and $x_c = 0.5$ is the initial location of the wave. The width of the Gaussian is controlled by $R_c = 20\Delta x$ ensuring a well resolved wave. Moreover, a mean flow U_x directed along the positive x-axis has been added corresponding to a Mach number of 0.1. Only the case of a wave propagating form the NS domain to the LBM domain is presented here as the results are the same for a wave propagating in the opposite direction.

The uniform grid size is set to $\Delta x = L/200$ and the time-step is chosen so as to enforce a CFL number based on the upstream velocity CFL $= 1/\sqrt{3} \approx 0.57$ for both the NS-FV and lattice Boltzmann solvers. Time integration on the NS-FV side will be performed with the 3^{rd}-order explicit Runge-Kutta scheme.

First of all, the influence of the thermodynamic closure derived in Section 3.3 is investigated. Two simulations are run: one where a constant temperature T_0 is specified at the NS-FV solver on the interface and another one taking into account the temperature fluctuations T' according to Equation (19). Indeed,

such reconstruction is valid in the present context since the temperature field in the NS solver has been initally computed according to the Laplace law for isentropic flows. Moreover, for air (i.e. with low viscosity and thermal conductivity) the entropy production can be neglected when propagating the wave over small distances of the order of L. Both computations are run until the acoustic wave reaches the interface between both solvers. Figure 5 compares the corresponding relative density profiles $(\rho - \rho_0)/A$. It can be seen that when applying a constant temperature, spurious oscillations appear in the density and temperature fields on the Navier-Stokes side. By contrast, the lattice Boltzmann solver is unaffected by these oscillations since no equation for energy conservation is solved with a D3Q19 lattice. On the other hand, thanks to the temperature fluctuations estimation presented in Section 3.3, a smooth transition is recovered. Indeed, the density profile remains continuous across the interface between both numerical methods and the solution perfectly matches the analytical one. Therefore, only computations taking into account the reconstructed temperature fluctuations will be shown hereafter.

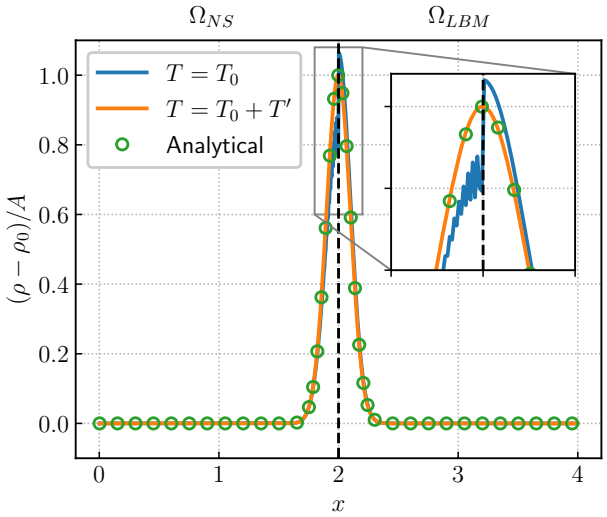

Figure 5: Relative density profile $(\rho - \rho_0)/A$ for the $1D$ convected acoustic wave test case. Two computations are compared: one where a constant temperature T_0 is specified at the NS-FV solver on the interface and another one taking into account the temperature fluctuations T' according to Equation (19).

The reconstruction of distribution functions is now considered. Again, two simulations are run: one where the LB distribution functions are specified to their equilibrium value at the interface and another one taking into account the off-equilibrium contribution $g_i^{neq,(1)}$ given by Equation (24). As previously, the computations are run until the acoustic wave reaches the interface between both solvers. This comparison has been motivated by previous results [14, 59] where the authors pointed out the importance of considering the off-equilibrium part. In Figure 6 the corresponding relative density profile and the density gradient are shown. While in Figure 6a both reconstructions seem to lead to a satisfying result matching the

analytical solution, further analysis highlights some discrepancies. Indeed, the density gradient exhibits a non-smooth behaviour in the vicinity of the coupling interface when distribution functions are reconstructed using only their equilibrium value. Over time, i.e. after many crossings of the interface, the waveform is eventually strongly degraded. In comparison, taking into account more macroscopic information through the off-equilibrium contribution $g_i^{neq,(1)}$ enables to recover a smooth gradient which perfectly matches the analytical one. As a consequence, one can conclude that the off-equilibrium contribution is necessary to obtain the correct profiles and thus the correct acoustics. This result, largely demonstrated in the stationary case [14, 59], is therefore also verified in the unsteady case. As a consequence, the off-equilibrium contribution is always applied in the following computations.

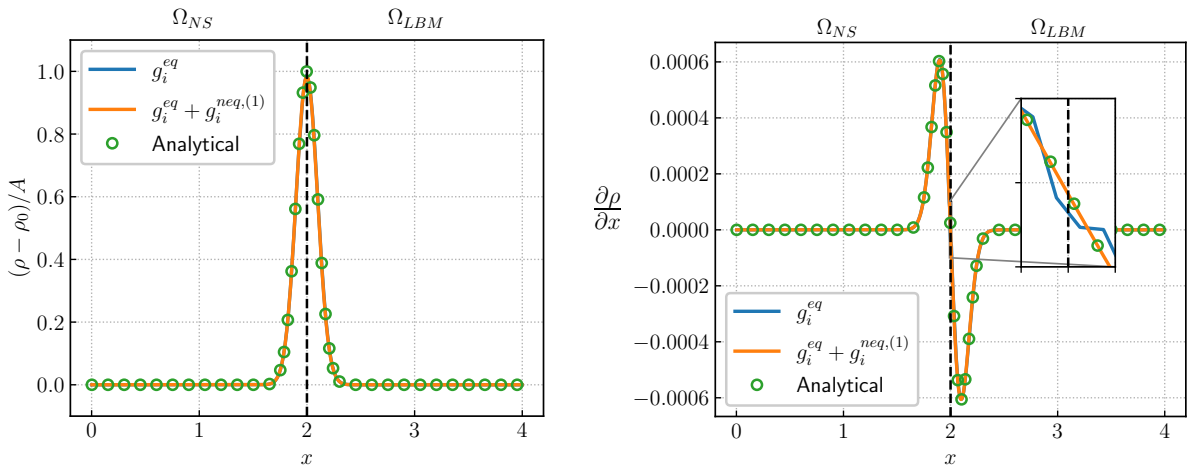

(a) (b)

Figure 6: (a) Relative density profile $(\rho - \rho_0)/A$ and (b) Density gradient for the $1D$ convected acoustic wave test case. Two computations are compared: one where the LB distribution functions are specified to their equilibrium value at the interface and another one taking into account the off-equilibrium contribution.

To complete this discussion on the different coupling components introduced in Section 3, the influence of the time interpolation and of the order of the Lagrange interpolating polynomials is now studied. Figure 7a displays the relative density profile $(\rho - \rho_0)/A$ after the first interface crossing for all the interpolation orders considered. Regardless of the choice made concerning the order of the Lagrange polynomial, the solution compares well with the analytical solution. However, some spurious acoustic waves, highlighted by a rectangular box, are reflected at the coupling interface and travel upstream. Figure 7b provides a closer look to them. First thing to notice is that the amplitude of these spurious waves represent less than 0.1% of the incident physical wave. More interestingly, this figure helps to characterise the overall effect of the interpolation order: by increasing the set of points used for the interpolation – and thus the order of the Lagrange polynomial – the amplitude of the spurious reflected waves is significantly reduced. Since both

the third- and fourth-order interpolation lead to similar results, one can conclude that there is no need to employ higher-order polynomials. Using a 3rd-order Lagrange polynomial interpolation eventually leads to a reflected wave representing less than 0.025% of the amplitude of the incoming wave which is considered as being acceptable (Figure 8 shows their negligible effect on the overall computation after 10 advection cycles). The interpolation process having converged, the remaining spurious acoustics are expected to arise from the change in numerical methods. As a complement, Figure 7c presents the evolution of the L_2 density error integrated over the whole computational domain as a function of the iteration number. The two vertical dashed lines represent the instant when the pulse starts (and respectively ends) crossing the coupling interface. On this Figure, two kind of errors are noticeable. The first one corresponds to the numerical error of each scheme. Indeed, before the first dashed line, the L_2 error constantly increases owing to the numerical dissipation of the Navier-Stokes solver. On the other hand, and in agreement with the results of [7], the LB solver exhibits a lower numerical dissipation of the acoustic wave since the L_2 error tends to remain constant over time. The other error component which is evidenced between the two dashed lines is to one arising from the crossing of the acoustic pulse through the coupling interface. As one might expect in the light of the previous Figures, increasing the interpolation order tends to smooth-out the error peaks which clearly indicate the presence of spurious emissions.

More interestingly, the order of the Lagrange interpolating polynomials fully conditions the error level after the coupling interface crossing, and by increasing the latter, the L_2 density error is diminished. Once again, the results are more or less the same whether we take an interpolation of order 3 or 4. As consequence, only 3^{rd}-order temporal interpolations will be considered in the following as the spurious acoustics can be seen as negligible in comparison with the physical acoustic phenomenon simulated.

In order to get a more quantitative insight into the influence of each of the coupling components, Table 3 provides the values of the L^2 density error after one interface crossing (i.e. when the acoustic wave reaches the center of the LBM domain). In Table 3, the first two columns indicate whether the temperature reconstruction or the off-equilibrium contribution of the distribution functions are taken into account (✓) or not (✗) whereas the other columns refer to the order of the time interpolation. The L^2 density error is defined as:

$$L^2(\rho) = \sqrt{\sum_{N_x,N_y,N_z} [\rho(x,y,z) - \rho_{\text{ana}}(x,y,z)]}, \tag{31}$$

where N_x, N_y, and N_z are the number of grid points in the computational domain along the x, y, and z axes respectively. The analytical density field is denoted by ρ_{ana}.

By comparing the first two lines of Table 3 with the last two ones, it can be seen that it is crucial to reconstruct the temperature fluctuations at the coupling interface. Indeed, regardless of the order of the time interpolation, the computations where only the reference temperature T_0 is imposed at the coupling interface exhibit an error larger of one order of magnitude compared to the ones where the temperature

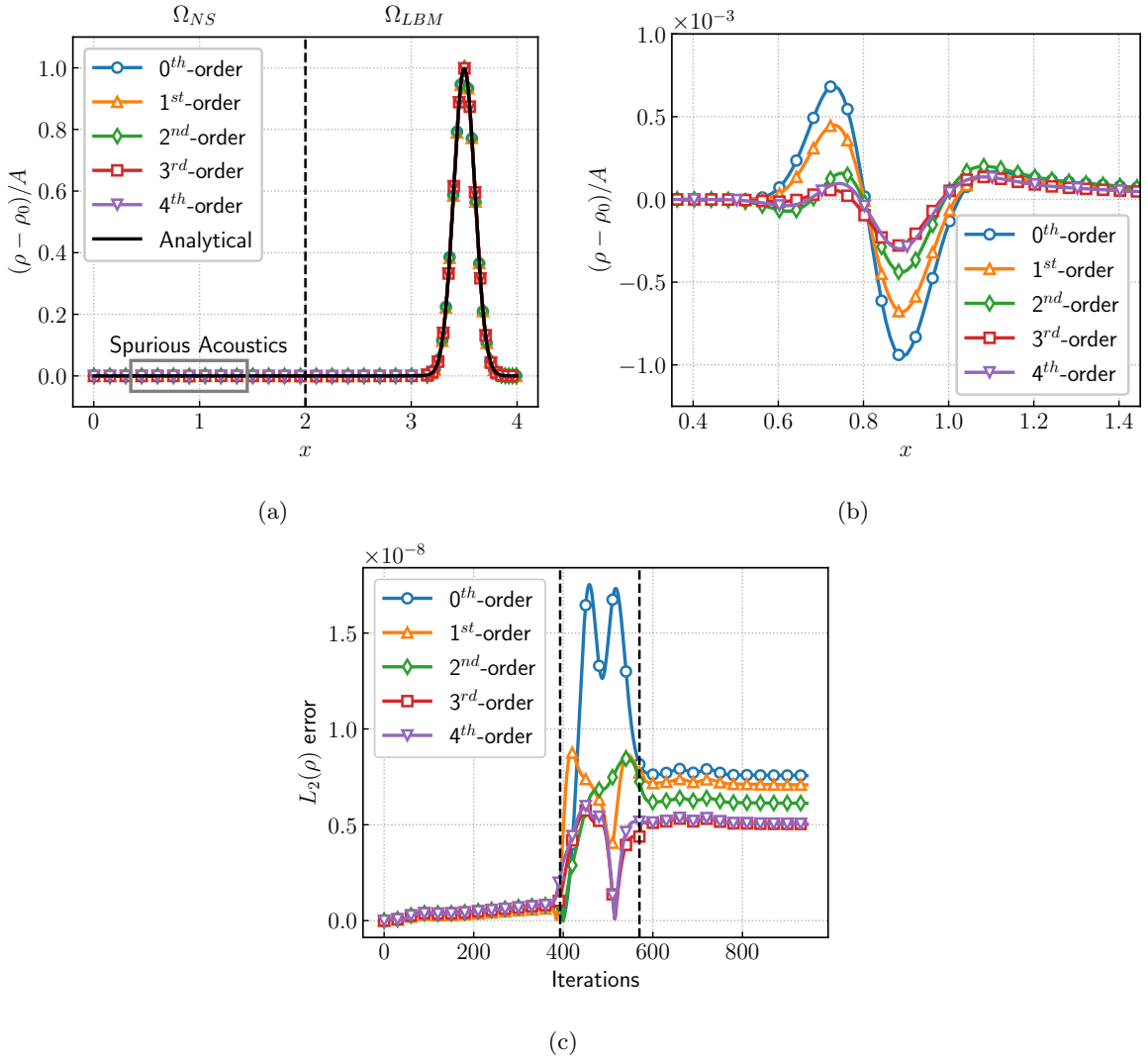

Figure 7: Influence of the interpolation order on spurious acoustics. (a) Relative density profile, (b) Zoom on spurious acoustic waves, (c) L_2 error as a function of iteration number.

T'	$g_i^{neq,(1)}$	0^{th}-order	1^{st}-order	2^{nd}-order	3^{rd}-order	4^{th}-order
✗	✗	3.189×10^{-7}	3.132×10^{-7}	3.068×10^{-7}	2.950×10^{-7}	2.898×10^{-7}
✗	✓	3.180×10^{-7}	3.093×10^{-7}	2.982×10^{-7}	2.858×10^{-7}	2.803×10^{-7}
✓	✗	1.097×10^{-8}	1.073×10^{-8}	1.041×10^{-8}	1.019×10^{-8}	0.984×10^{-8}
✓	✓	7.563×10^{-9}	7.089×10^{-9}	6.116×10^{-9}	5.046×10^{-9}	5.039×10^{-9}

Table 3: L^2 density error after one interface crossing of the acoustic wave. The effects of the temperature fluctuations reconstruction, the off-equilibrium contribution and the time interpolation are investigated.

fluctuations are reconstructed through Equation (19). In addition, comparing the first two lines of Table 3 shows that the error due to an incorrect thermodynamic closure is prevalent since adding the off-equilibrium contribution to the distribution functions has little effect on the level of the L^2 error. Consequently, the positive effect of taking into account the off-equilibrium contribution in the distribution functions is only highlighted once the thermodynamic closure is properly addressed. This is shown in the third line of Table 3 where a twofold reduction in the L^2 error is observed when the off-equilibrium is taken into account. Finally, Table 3 also confirms the results of Figure 7: increasing the time interpolation order helps in reducing the error level at the end of the computation. It can be noted that the L^2 errors in the last line of Table 3 are exactly the same as the ones shown in Figure 7c.

To conclude the analysis of this test case, the stability and robustness of the coupling procedure are discussed by performing the computation over 10 advection cycles. As shown by the last line of Table 3, the use of a fourth-order time interpolation does not lead to a significant reduction in error compared to third order interpolation. Therefore, only 0^{th}- to 3^{rd}-order time interpolations are considered in the following.

Table 4 provides the values of the L^2 density error after 10 advection cycles. Overall, the conclusions reached in the study of Table 3 are also confirmed after 10 advection cycles. It is important to note that the value of the temperature correction introduced in Section 3.3 is exacerbated after 10 advection cycles insofar as the error is two orders of magnitude greater in the cases where this correction is not taken into account. Besides, the last line of Table 4 demonstrates the robustness of the coupling procedure when taking into consideration the temperature fluctuations and the off-equilibrium contribution reconstructions at the interface between both methods. Indeed, while the error values are slightly higher than in Table 3 (mainly due to dissipation as shown by Figure 8), they seem to remain bounded which proves that the coupling error does not lead to an accumulation that could compromise the stability and quality of the solution.

T'	$g_i^{neq,(1)}$	0^{th}-order	1^{st}-order	2^{nd}-order	3^{rd}-order
✗	✗	5.399×10^{-6}	5.384×10^{-6}	5.352×10^{-6}	5.321×10^{-6}
✗	✓	5.288×10^{-6}	5.272×10^{-6}	5.238×10^{-6}	5.206×10^{-6}
✓	✗	6.562×10^{-8}	5.498×10^{-8}	4.1630×10^{-8}	3.246×10^{-8}
✓	✓	3.063×10^{-8}	2.853×10^{-8}	2.369×10^{-8}	1.892×10^{-8}

Table 4: L^2 density error after 10 advection cycles of the acoustic wave.

To substantiate these statements, Figure 8 shows the corresponding relative density profile and the density gradient after 10 advection cycles when both the temperature fluctuations and the off-equilibrium contributions reconstructions are considered. It can be seen that, even after many crossings of the interface, the waveform is preserved and perfectly matches the analytical profile. Furthermore, the spurious acoustic

waves induced by the coupling interface do not build up and remain unnoticeable at the scale of the initial perturbation. Moreover, Figure 8b focuses on the density gradient. Thanks to the off-equilibrium contribution $g_i^{neq,(1)}$, the gradient is also in good agreement with the its analytical counterpart and very limited spurious oscillations are exhibited. In addition to the computation over 10 advection cycles, another one over 100 advection cycles is also performed and the amplitude of the spurious waves is still found to be negligible (of the order of 1% of the acoustic wave). Consequently, it can be concluded that the coupling strategy remains stable despite the minor errors generated at the interface between both numerical methods.

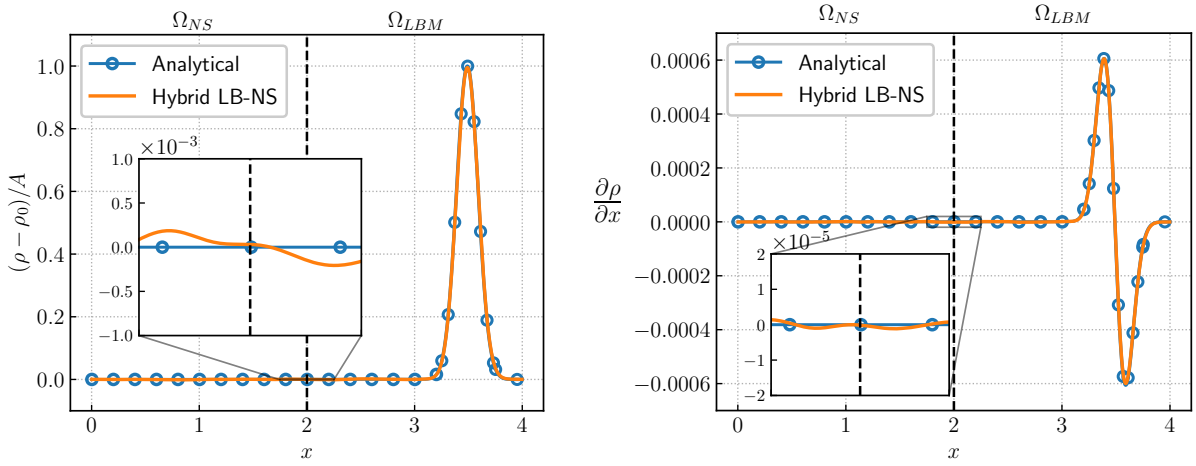

(a) (b)

Figure 8: (a) Relative density profile $(\rho - \rho_0)/A$ and (b) Density gradient for the $1D$ convected acoustic wave test case after 10 advection cycles. In the present computation, both the temperature fluctuations and the off-equilibrium contributions are used. In addition, a third-order time interpolation is employed.

4.2. Convected vortex

The convected vortex is a classic Euler benchmark which is often used in the context of computational fluid dynamics to assess numerical schemes in terms of dispersion, dissipation, and robustness. As discussed in dedicated publications [62, 63], care has to be taken at the initialisation stage when using the lattice Boltzmann method. Indeed, the classical isentropic formulation of the convected vortex test case is not consistent with the athermal approximation of standard LBMs since in such approaches no energy conservation equation is solved. An improper inital field can then lead to strong spurious waves compromising the entire computation. To alleviate this issue, a more suited "barotropic" version of the widely used Taylor vortex

derived in [63] is chosen. It reads:

$$\begin{cases} \rho(x,y) &= \rho_0 \exp\left[-\dfrac{\epsilon^2}{2c_s^2}\exp\left(\dfrac{-r^2}{R_c^2}\right)\right], \\ u_x(x,y) &= U_0 - \epsilon\left(\dfrac{y-y_c}{R_c}\right)\exp\left[-\dfrac{(x-x_c)^2+(y-y_c)^2}{2R_c^2}\right], \\ u_y(x,y) &= \epsilon\left(\dfrac{x-x_c}{R_c}\right)\exp\left[-\dfrac{(x-x_c)^2+(y-y_c)^2}{2R_c^2}\right], \end{cases} \tag{32}$$

where $\rho_0 = 1.1765$ kg.m^{-3} is the free-stream density, $U_x = 0.1c_0$ is the advection speed, $\epsilon = 0.07c_0$ is the vortex strength, and $R_c = 0.1$ m is the characteristic radius of the vortex. The center of the vortex is initially positioned at (x_c, y_c). The corresponding analytical solution is given by the exact same pattern simply advected by the mean flow over time.

The computational domain, which is shown in Figure 9, is a box of size $[3L, L, 10\Delta x]$ decomposed in 3 sub-domains of size $[L, L, 10\Delta x]$ each, with L being the reference length equal to 1 m. Two NS sub-domains, located at each side of a LBM sub-domain, enable to study the two-way crossing of vortical structures. Periodic boundary conditions are implemented at the borders of the computational domain in all three directions of space.

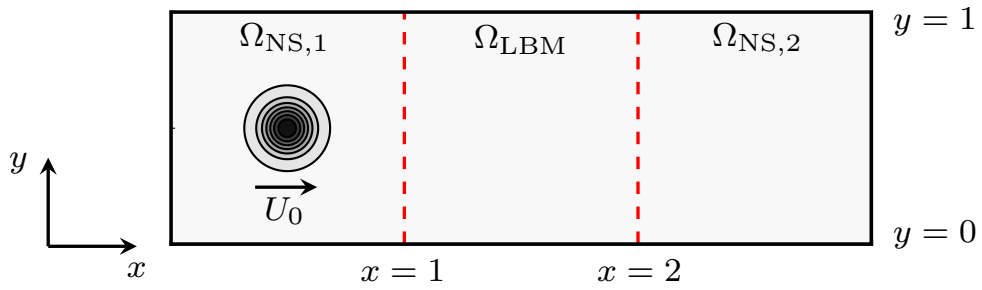

Figure 9: Schematic representation of the computational domain for the convected vortex test case.

The uniform grid size is set to $\Delta x = L/N$ where N is the number of grid points per unit length and the time-step is chosen so as to enforce a CFL number based on the upstream velocity CFL $= 1/\sqrt{3} \approx 0.57$ for both the NS-FV and lattice Boltzmann solvers thus ensuring a synchronous evolution. In the following, the grid resolution is fixed to $N = 200$ unless otherwise stated leading to 20 cells in the radius of the vortical structure. Moreover, this test case is performed in the inviscid limit to get rid of the viscous dissipation and directly investigate the numerical dissipation of the hybrid method. This also allows to study the stability of the hybrid method. As a consequence, only convective fluxes will be evaluated by the FV solver and the LB relaxation time is set to $\overline{\tau} = 0.5$.

First, the results obtained with the NS-FV method equipped with the 3^{rd}-order explicit Runge-Kutta scheme are presented. Figure 10 shows the relative density and velocity profiles for the first (Figure 10a)

and tenth (Figure 10b) advection cycles respectively at five different stages. One should notice that, one advection cycle refers to the time needed for the vortex to be advected back to its initial position.

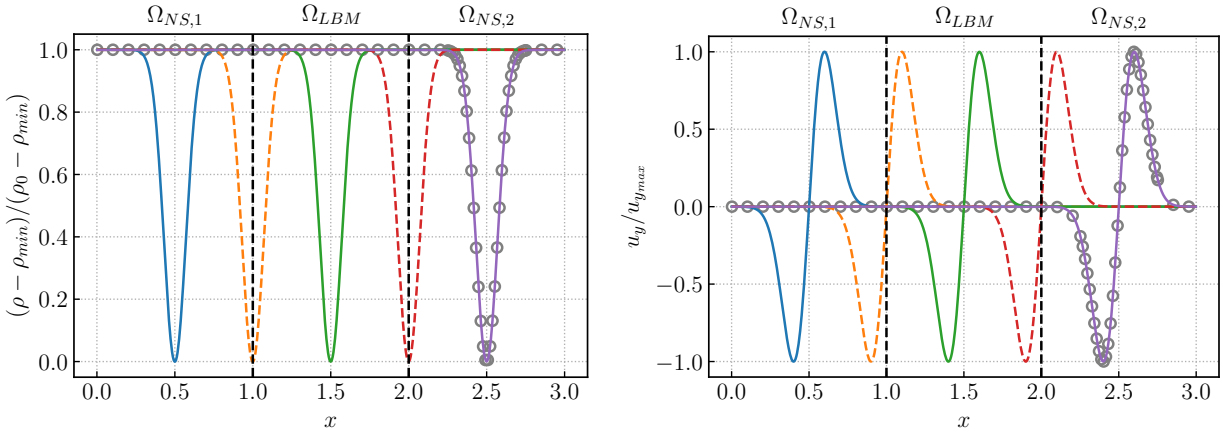

(a) 1^{st} advection cycle, $t_0^\star = 0$

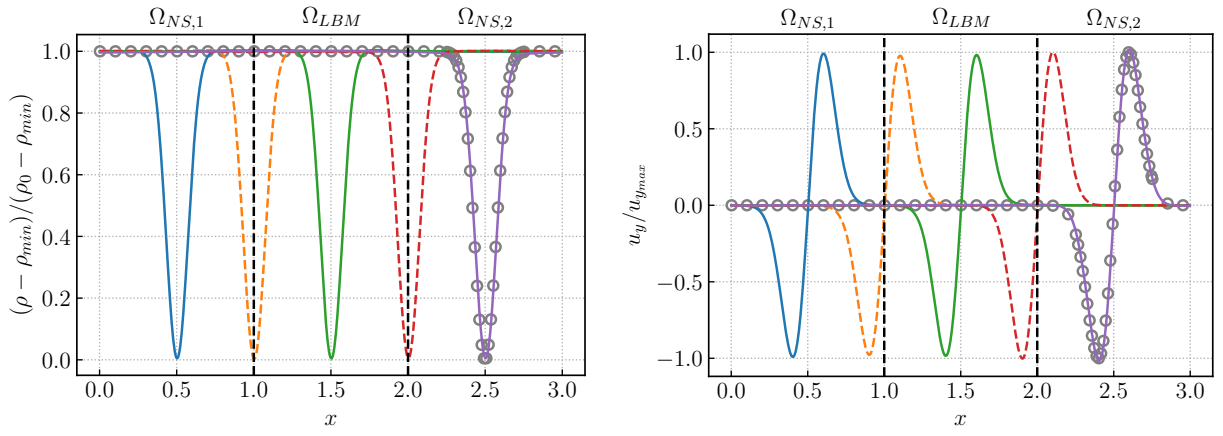

(b) 10^{th} advection cycle, $t_0^\star = 30$

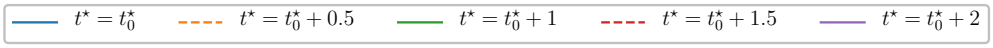

Figure 10: Density (left) and u_y velocity component (right) profiles for the periodic convected vortex for the (a) first and (b) tenth advection cycle. Time is expressed through its non-dimensional value $t^\star = t/T_{\text{covo}}$ where $T_{\text{covo}} = N/U_0$. The analytical solution (○) is superimposed at $t^\star = t_0^\star + 2$.

It can be observed from Figure 10 that the vortex crosses the two coupling interfaces without any distortion: the shape of the vortex is preserved regardless of the number of advection cycles and no spurious oscillations are visible at the transitions between both solvers. Moreover, analytical profiles (indicated by circles ○) have been superimposed on Figure 10 and show that all the results are in good agreement with the analytical solution.

The numerical dissipation of the hybrid method is now quantified with the following parameter $\xi = \frac{\min \rho(t_0) - \min \rho(t_f)}{1 - \min \rho(t_0)}$. A value of $\xi = 8 \times 10^{-5}$ is obtained after 10 advection cycles meaning that less than 0.01%

of the initial amplitude is lost. Furthermore, the numerical dissipation is found to be $\xi = 3 \times 10^{-4} < 0.05\%$ after 30 advection cycles. As a consequence, the hybrid method has very little intrinsic numerical dissipation thanks to the combination of the hybrid centered/decentered convective fluxes in the NS-FV solver and the value of $\sigma = 0.995$ which is used for the HRR collision operator. This also indicates that the value of $\sigma = 0$ which is imposed in the LB ghost-cells by the coupling procedure has a negligible effect on the overall dissipation of the hybrid method. Note that a smaller value of σ can be chosen in the bulk solver to increase the stability however owing to the fact that computations remain stable after 50 advection cycles, it is concluded that the value of $\sigma = 0.995$ is sufficient to ensure stable results.

In order to get more insight into the results obtained with the hybrid lattice Boltzmann - Navier-Stokes method, the derivatives of the flow variables are computed. As indicated in [15], when coupling two numerical methods, the quality of the vorticity field is more sensitive than the velocity field at the interface. Indeed, vorticity, which is defined by $\boldsymbol{\omega} = \boldsymbol{\nabla} \times \boldsymbol{u}$, involves first-order derivatives of the velocity field. Consequently, ensuring its smoothness requires stricter conditions on the velocity field. To investigate this particular point, Figure 11 displays the vorticity field in the vicinity of the first coupling interface (i.e. the one between $\Omega_{\mathrm{NS},1}$ and Ω_{LBM}) after 10 advection cycles.

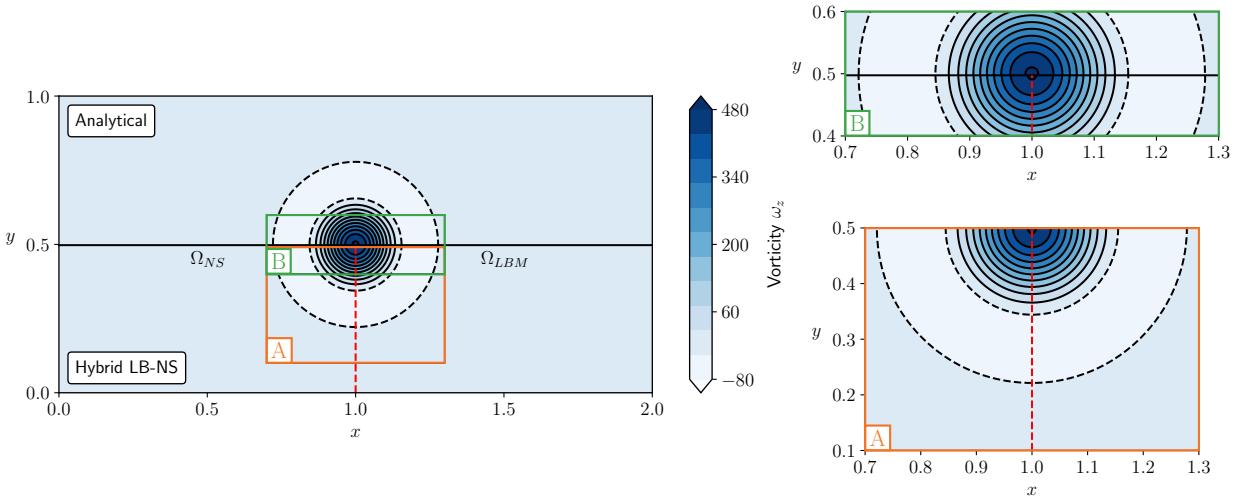

Figure 11: Vorticiy field in the vicinity of the first coupling interface (centered at location $x = 1$). Iso-contours of vorticity are displayed. The countour levels are from $\omega_{min} = -80$ to $\omega_{max} = 480$ with an increment of 46.—— : $\omega > 0$ and - - - : $\omega < 0$.

The vorticity field shown on Figure 11 is split in two: the upper half corresponds to the analytical vorticity field while the lower half represents the one computed by the hybrid method. Moreover, 12 iso-contours evenly spaced between $\omega_z = -80$ s^{-1} and $\omega_z = 480$ s^{-1} have been superimposed to the vorticity fields. The results indicate that the isotropy of the solution is preserved. In addition, all contours are continuous and do not exhibit any oscillations nor abrupt slope changes. Consequently, one can conclude that the proposed

coupling strategy not only guarantees continuous velocity fields but also a continuous vorticity field across the interface between both solvers.

Different cases with the mean flow spanning all three axis major directions and diagonals have been tested and have shown similar results to those of Figure 10 and Figure 11 thereby validating the 3D implementation of the hybrid method.

As the coupling strategy is validated with an explicit time advance scheme for the NS-FV side, the coupling between the LBM with a NS-FV solver relying on an implicit time scheme is now analysed. The exact same computational domain as the one presented in Figure 9 is considered. Both the grid size and the time step (and thus the CFL number) remain unchanged. The aim is not only to validate the LBM/implicit coupling but also to characterise the effect of the numerical errors induced by the explicit treatment of the boundary conditions (see Section 3.5.2). The computations are therefore compared to their hybrid LBM - NS-FV explicit counterpart so as to only highlight the effect of changing the time-marching method. As stated the implicit scheme involves Newton sub-iterations. Therefore, the influence of the convergence criteria is also investigated. .

On Figure 12, the relative density profile and the error $\rho(x,y) - \rho_{\text{ref}}(x,y)$ at $t^\star = 4.5$ are plotted. The computation is stopped when the vortex crosses the $\Omega_{\text{LBM}} \rightarrow \Omega_{\text{NS},2}$ interface to clearly highlight the boundary treatment in the LBM/implicit time coupling. Three values of sub-iterations number are considered namely 3, 7, and 20. These, equivalently, correspond to an L_∞ norm of the Newton residual ϵ of 10^{-1}, $10^{-2.2}$, and 10^{-5} respectively.

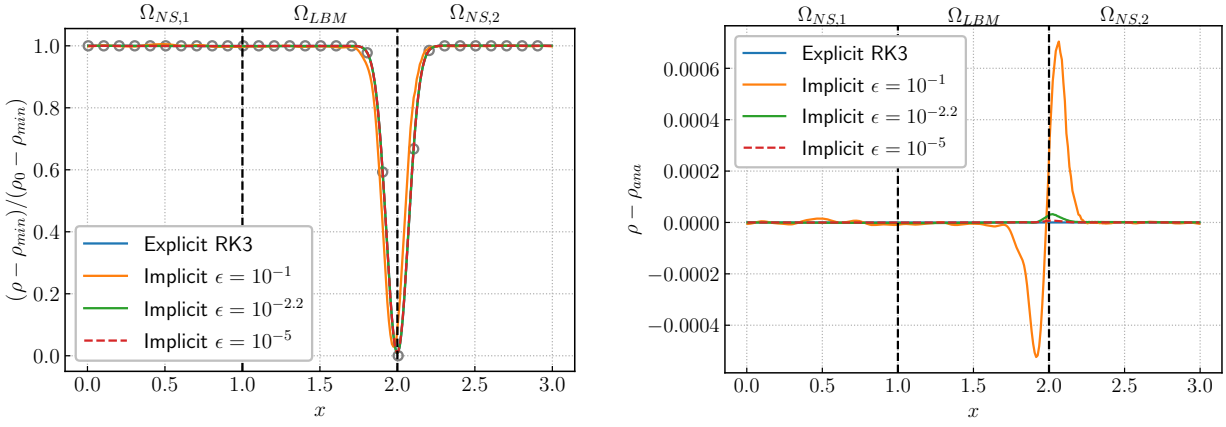

(a) (b)

Figure 12: Density (a) and density error (b) profiles for the periodic convected vortex with an implicit time scheme for the NS-FV solver. The analytical solution (○) is superimposed on (a).

As evidenced by Figure 12a, an insufficient number of sub-iterations ($\epsilon = 10^{-1}$) leads to significant

numerical dissipation and dispersion errors. In fact, the error which is reported on Figure 12b reflects this phenomenon. Naturally, decreasing the value of ϵ tends to improve the solution. The parameter ϵ has to be small enough to damp out the spurious effect of the explicit treatment of the boundary conditions in the Newton process. For the convected vortex test case, $\epsilon = 10^{-5}$ seems to be sufficient as the solution is almost perfectly superimposed on the explicit and the analytical ones (indicated by circles ○). Convergence to machine accuracy is not required. Moreover, as in the explicit case, the vorticity remains continuous at the interface between the NS-FV and LBM solvers when using the implicit time stepping.

Yet, one has to notice that on this particular test case, in order to achieve the same level of accuracy, the implicit method is less computational efficient than the explicit one. However, as will be seen in Section 4.4, using an implicit time integration scheme for the NS-FV solver can be beneficial when doing computations on domains with a large disparity of grid sizes.

The convergence order of the hybrid lattice Boltzmann - Navier-Stokes method on the convected vortex test case, is now determined. Knowing the exact solution at any given time, the error between the simulation result and the translated initial conditions can be easily computed. For any flow quantity q, the relative L^2 error is defined as:

$$L^2(q) = \sqrt{\frac{1}{N_x N_y N_z} \frac{\sum_{x,y,z} [q(x,y,z) - q_{ref}(x,y,z)]}{\sum_{x,y,z} q_{ref}(x,y,z)}}, \tag{33}$$

where N_x, N_y, and N_z are the number of grid points in the computational domain along the x, y, and z axes respectively. The exact value of the flow quantity q is denoted by q_{ref}.

The convected vortex test case is conducted on the computational domain of Figure 9 for a range of grid resolution N with $N \in \{25, 50, 100, 200, 400\}$. For each value of N, the vortex is advected for 10 cycles and both the density and velocity L^2 errors are computed. Figure 13 shows the x-velocity L^2 error versus the vortex resolution (i.e. the number of grid points in the radius of the vortical structure $R_c = N/10$) for the hybrid method as well as for a full Navier-Stokes and a full LBM computation using the exact same grid and time steps. A second-order reference slope is also added to the plot to ease the interpretation of the results.

The first thing to notice is that the classical second-order convergence of the LBM [64] is retrieved. In comparison, the Navier-Stokes Finite-Volume solver seems to have a spatial order higher than 2. This is due to the fact that all the computations are run using the time-step defined by Equation (9). Thus, changing the vortex resolution also affects the time step. As a consequence, the slope obtained by the NS solver is greater than 2 owing to the 3rd order convergence rate of the explicit Runge-Kutta scheme. When using the implicit Gear scheme, which is second order in time, a slope of 2 is recovered. This being said, the general conclusion of [7] is also recovered: at low resolutions ($N = 25$ or $N = 50$), the lattice Boltzmann method is more precise than the NS-FV method because of its low numerical dissipation.

Moving now to the analysis of the hybrid method, one can see that for all vortex resolutions, the L^2

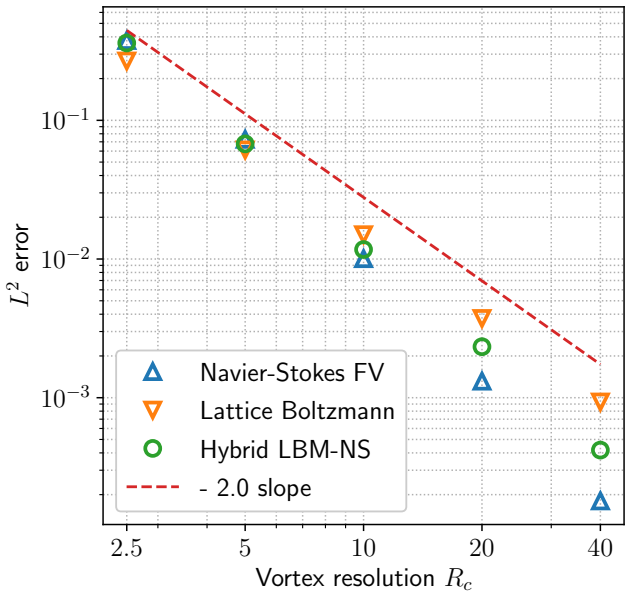

Figure 13: Convergence rate study of the proposed hybrid lattice Boltzmann - Navier-Stokes method. The relative error is computed through L^2 error on the x-velocity component after 10 advection cycles.

error always lies between the one of the LB solver and the one of the NS-FV solver. By comparison with the reference second-order slope, it becomes clear that the coupled method has a second order convergence rate. Notwithstanding the fact that only the x-velocity L^2 error is represented on Figure 13, the same results are obtained for all the others flow quantities. This result is in accordance with previous studies [13, 59].

4.3. Harmonic acoustic source radiation in a fluid medium at rest

The hybrid lattice Boltzmann - Navier-Stokes method is now assessed on an acoustic propagation problem. This constitutes a first step towards the computation of realistic cases were the source is resolved with one method whereas the other one is used to propagate the acoustic waves. Indeed, it is of paramount importance to evaluate the acoustic capabilities of a numerical scheme in the field of computational aeroacoustics. The acoustic quantities being several orders smaller than their aerodynamic counterparts, the hybrid method should be able to propagate acoustic waves accurately over long distances with very low numerical noise. The aim of this test case is to study the suitability of the hybrid solver to perform acoustic computations and to characterise its dissipation and dispersion errors.

In a fluid medium at rest (characterised by $\rho_0 = 1.1765$ kg.m^{-3} and $p_0 = 101320$ Pa), a harmonic

acoustic source is modeled by a source term $\mathbf{S}$ which is added to the right hand side of Equation (1):

$$\mathbf{S}(x,y,t) = A\sin(2\pi f_s t)e^{-\alpha\left(x^2+y^2\right)}\begin{pmatrix}1\\0\\0\\0\\c_0^2,\end{pmatrix} \tag{34}$$

The shape of the Gaussian source is controlled by $\alpha = \ln 2/4$. In the following, the frequency is fixed to $f_s = 72$ Hz leading to a wavelength of $\lambda = c_0/f_s = 4.77$ m. The source can then be seen as being acoustically compact since $\alpha/\lambda \ll 1$. Moreover, low and high acoustic levels are investigated with a sound pressure level (SPL) of 84 and 144 dB at the edge of the source corresponding to an amplitude of $A = 1\times10^{-3}$ and $A = 1$, respectively. As the source term corresponds to linear acoustics, the two sound levels are chosen in order to consider pressure fluctuations which differ by several orders of magnitude.

The computational domain, represented on Figure 14, consists in box of size $[42\lambda, 42\lambda, 10\Delta x]$ split into 9 sub-domains of size $[14\lambda, 14\lambda, 10\Delta x]$ each. Again, periodic boundary conditions are implemented in all directions. The acoustic source, centered at the origin of the domain (i.e. at $(x_s, y_s) = (0, 0)$), will be generated and computed by the Navier-Stokes finite-volume solver. Owing to its advantageous acoustic capabilities, the lattice Boltzmann method [7] will be employed in the farfield.
It can be mentioned that the role of each solver can be freely chosen and that different configurations of the NS and LBM zones have been tested leading to the same level of accuracy on a fine mesh. However, the hybrid lattice Boltzmann - Navier-Stokes method was found to be the most efficient for the domain decomposition shown in Figure 14. Therefore, only this configuration will be discussed hereafter.

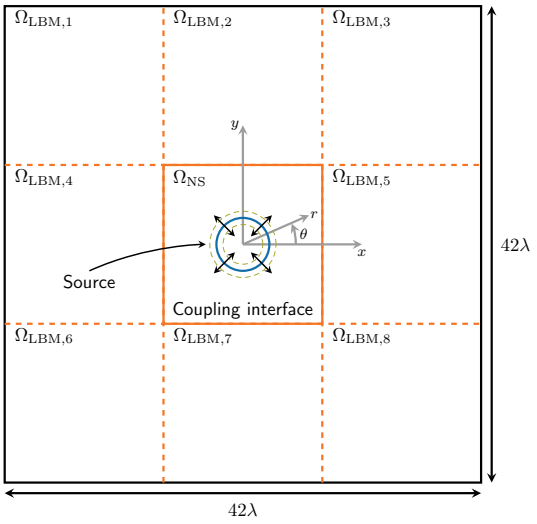

Figure 14: Schematic representation of the computational domain for the harmonic acoustic source radiation test case.

When running aeroacoustic computations, one fundamental parameter is the number of mesh points per wavelength $N_{\text{ppw}} = \lambda/\Delta x$. The second order hybrid centered/decentered scheme used to discretise the Eulerian fluxes in the FV solver requires about 15 to 20 points per wavelength in order to correctly propagate acoustic waves. Therefore, in the following, a uniform mesh size will be taken so as to ensure $N_{\text{ppw}} = 18$ throughout the entire computational domain. For both solvers, the time step will be set according to the acoustic scaling of Equation (9). Temporal integration will be carried out in the NS-FV solver by means of the 3^{rd}-order explicit Runge-Kutta scheme.

Figure 15, which shows the fluctuating pressure field (defined as $p' = p - p_0$) at three successive times, allows to visualise the propagation of the acoustic wave across the coupling interfaces. The figure is split in two parts where the analytical fluctuating pressure field is shown on the upper half and the one computed by the hybrid method is shown on the lower half. Iso-contours of $p' = 0$ have been superimposed so as to highlight the wave fronts. The computation is performed till $t = 18T$, where $T = 1/f_s$, to avoid acoustic interferences caused by the periodic boundary conditions.

From Figure 15, it can be deduced that the hybrid lattice Boltzmann - Navier-Stokes method provides good results. Indeed, the circular shape of the iso-contours, which is typical of the directivity of monopolar sources [54], indicates the isotropy of the scheme. In addition, no reflected waves have been generated at the coupling interface between the Navier-Stokes and lattice Boltzmann solver. This confirms that a 3^{rd}-order time interpolation is sufficient for the computation of acoustic test cases.

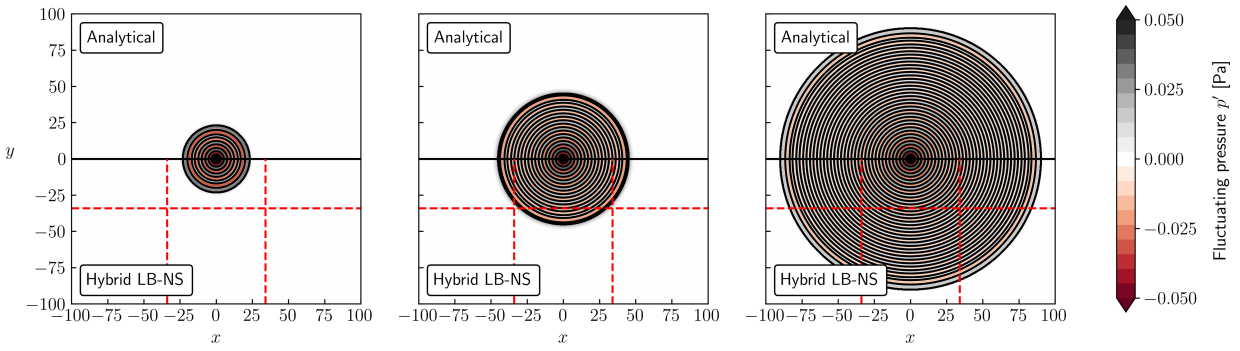

Figure 15: Temporal evolution of the fluctuating pressure field at $t = 4T$, $t = 9T$, and $t = 18T$ (from left to right). In the present case, the amplitude of the source is $A = 1 \times 10^{-3}$.

A first estimation of the numerical dispersion induced by the hybrid method can be obtained by tracking the position of the wave fronts along time. This way, one can obtain the numerical speed of sound which appears to be $c_{0,\text{num}} = 347.3$ m.s^{-1}. As this value is equal to its theoretical value $c_0 = \sqrt{\gamma R T_0} = 347.3$ m.s^{-1}, the dispersion effect on the speed of sound can be considered as negligible.

The analysis is now carried out by looking at the fluctuating pressure profile along the $y = 0$ and $x \geq 0$

line at the final time of the simulation (see Figure 16). The numerical result is also being compared to the analytical solution which is known for this case. Indeed, the pressure fluctuations at any point (x, y) in the far field are given by:

$$p'(x, y, t) = c_0^2 \rho'(x, y, t), \qquad \text{where} \qquad \rho'(x, y, t) = \frac{A}{\sqrt{kr}} \sin(\omega t - kr). \tag{35}$$

In equation (35), k is the wave number defined by $k = \omega/c_0 = 2\pi f_s/c_0$ and $r = |\boldsymbol{x} - \boldsymbol{x}_s|$ represents the distance of any point $\boldsymbol{x} = (x, y)$ to the source.

The good agreement between the numerical result of the hybrid method and the analytical solution can be observed in Figure 16 in both amplitude and frequency. Moreover, no discontinuity nor oscillations are observed in the vicinity of the interface thereby validating the information transfer for acoustic phenomena.

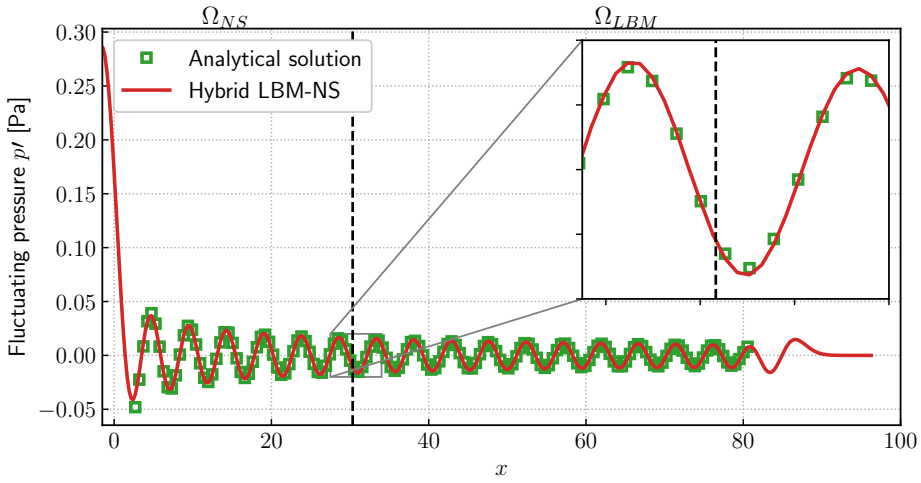

Figure 16: Fluctuating pressure profile along the $y = 0$ and $x \geq 0$ line at the final time of the simulation. The coupling interface is represented by the dashed line. In the present case, the amplitude of the source is $A = 1 \times 10^{-3}$.

The dissipation of acoustic waves is linked to the spatial amplitude decay of the waves. For a monopolar source in radiating in a 2D domain (the flow being homogeneous in the z direction), the decay theoretically follows a $1/\sqrt{r}$ law. In order to characterise the numerical dissipation of the method, the pressure fluctuations amplitude peaks along the $y = 0$ and $x \geq 0$ line are reported in a log-log plot as a function of $\sqrt{r}$ in Figure 17. Both sound pressure levels are considered and a linear fitting indicates that the points are all aligned following a slope of -1. Consequently, the classical $1/\sqrt{r}$ cylindrical decay is recovered for moderate to loud acoustic radiation. Moreover, by comparing the wave amplitude with its theoretical value, the numerical dissipation is negligible in comparison with the viscous molecular damping.

The propagation of acoustic waves has been validated on a computational domain relying on a uniform mesh of 18 points per wavelength. However, as indicated in [7], the lattice Boltzmann method requires less points per wavelength compared to Navier-Stokes methods to correctly propagate acoustic modes. In light

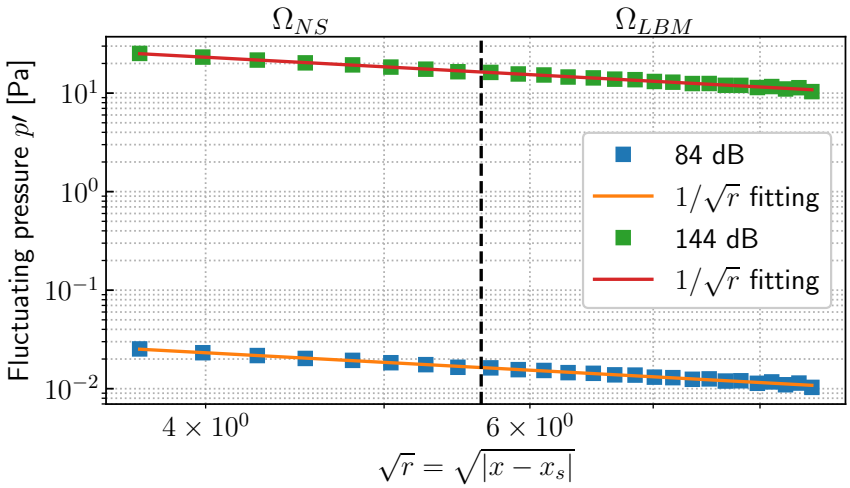

Figure 17: Radial decay of pressure waves for two different sound pressure levels.

of this conclusion, one might be interested in taking advantage of the hybrid lattice Boltzmann - Navier-Stokes method to reduce the cost of acoustic computation. Therefore, the exact same test case will now be computed on a grid where the NS sub-domain and LB sub-domains have a resolution of $N_{\text{ppw}} = 24$ and $N_{\text{ppw}} = 12$, respectively. The resulting computational domain contains 3 times less points with respect to its uniform counterpart. The aim of this short study is to verify the ability of the coupled solver to properly resolve acoustics while lowering the computational cost.

Figure 18 shows the result of 3 computations: a well-resolved full NS computation (with 24 mesh points per wavelength), an under-resolved full NS computation (with 12 mesh points per wavelength), and the hybrid lattice Boltzmann - Navier-Stokes computation on the hybrid mesh priorly introduced. In addition, results will also be compared to the analytical solution of Equation (35). Figure 18a represents the fluctuating pressure profile along the $y = 0$ and $x \geq 0$ line at the final time of the simulation. At the bottom of Figure 18a, an overview of the mesh has been added. In the present case, since only 1-to-1 coupling interfaces have been implemented, the change of resolution is performed in the NS domain just before the interface.

As expected, the under-resolved NS simulation over-damps the acoustic waves w.r.t. the analytical solution due to the insufficient resolution. By doubling the number of points per wavelength in each direction, the full NS computation retrieves the analytical amplitude decay. However, the most interesting result is provided by the hybrid computation which has 3 times less mesh points than the ones needed for the resolved NS computation. Thanks to the low dissipative property of the LBM, keeping only 12 points per wavelength after the coupling interface is sufficient to properly propagate the sound waves. Figure 18b provides a more detailed view of the different solutions in the far-field, i.e. for $x > 10\lambda$, where it can be seen that the hybrid method leads to a huge improvement in terms of dissipation. However, there is a slight dispersive effect, as is expected for lattice Boltzmann methods [7]. The latter can be quantified and leads to a frequency shift of 0.1

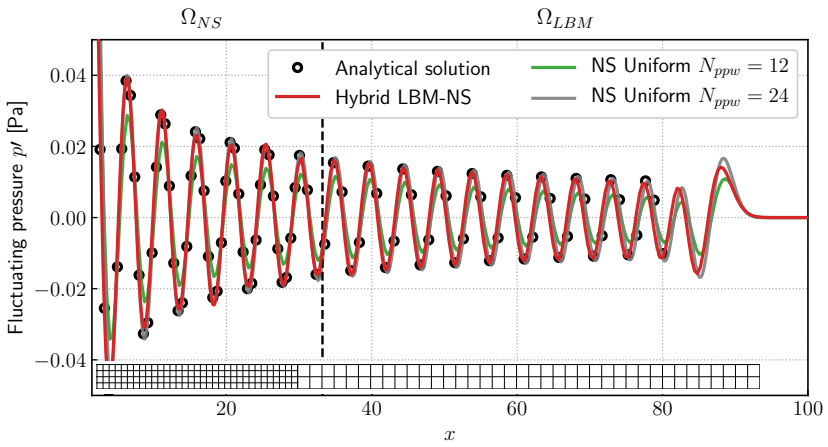

(a)

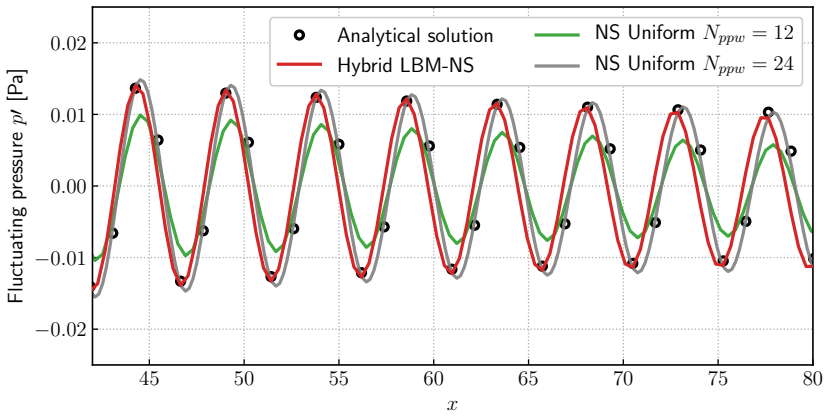

(b)

Figure 18: Fluctuating pressure profile along the $y = 0$ and $x \geq 0$ line at the final time of the simulation in the case of a non-uniform mesh. The coupling interface is represented by the dashed line. The amplitude of the source is $A = 1 \times 10^{-3}$.

Hz which is acceptable in light of the improvement in terms of dissipation. To conclude, the hybrid method is very promising when computing acoustic problems inasmuch as it helps to decrease the number of points per wavelength without deteriorating the solution. Even though this test case could have been computed entirely by the LBM, the following test case will show that when sources become more complex, the use of NS methods in these regions can bring in an improvement with respect to full LBM computations.

4.4. Circular cylinder in an uniform viscous flow

The last test case proposed in this paper is the study of the sound generated by a circular cylinder in a uniform flow. Despite the simple geometry of the obstacle, this test case is still demanding with regard to the quality of the aerodynamic and acoustic results. Besides, the large disparity between the aerodynamic

and acoustic characteristic length scales makes the direct numerical simulation of both the aerodynamics and acoustics a challenging task in terms of meshing and computational cost.

In the following, the proposed hybrid lattice Boltzmann - Navier-Stokes method is compared to full NS-FV and LBM-HRR computations. While the former are performed using ONERA's CFD suite, the full LBM-HRR simulation is based on the ProLB commercial solver [65]. Indeed, ONERA's lattice Boltzmann module is unable to handle multi-resolution computations in its current version preventing simulations from being carried out at an industrial level. The choice of the ProLB sofware is thereby motivated by the fact that it relies on the same core components as the ones presented in Section 2.2.

The aim is to rigorously compare the CPU efficiency of each approach when performing the direct numerical simulation of both the aerodynamics and acoustics simultaneously. From an engineering point of view, the case was set up for each solver such as to provide an error of 5%, at most, in the estimation of the aerodynamic forces and the sound pressure level (SPL) at a distance of $150D$ of the source.

The flow configuration of Inoue and Hatakeyama [66] is considered. A cylinder of diameter $D = 1$ m is fixed in a uniform flow. The upstream Mach number M_∞ is set to $M_\infty = 0.2$ and a Reynolds number $Re = U_\infty D/\nu_\infty$ of 150 is chosen in order to remain below the onset of three-dimensional fluctuations and turbulent behavior [67]. Since the Mach number is relatively low, temperature dependence of the the molecular viscosity is not likely to have a significant effect and therefore the latter is taken at a constant value. The flow configuration is shown in Figure 19.

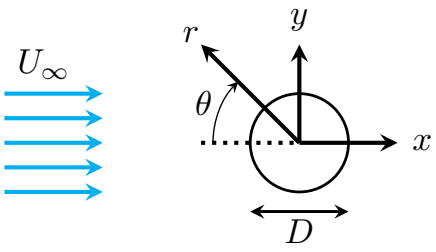

Figure 19: Flow configuration and notations for the study of the flow over a circular cylinder.

The computational domain has a size of $[600D, 600D, 10\Delta x]$ and the cylinder is centered at its origin. As seen in Figure 20, two types of grids are currently used. The first one, shown in Figure 20a, relies on a hybrid mesh consisting of curvilinear and Cartesian cubic blocks. It is used for both the hybrid lattice Boltzmann - Navier-Stokes and full Navier-Stokes computations. The second one is a Cartesian cubic grid, which was automatically generated by ProLB's octree mesher, is used for the full lattice Boltzmann computation and is shown in Figure 20b. Adiabatic no-slip boundary conditions are used for the cylinder surface and periodic boundary conditions are applied in the z direction. In addition, non-reflecting far-field boundary conditions are imposed 300 diameters away from the cylinder in the x and y directions. These boundary conditions

are applied in different ways depending on the computations. For the hybrid and full-NS simulations, they rely on the formalism introduced by Thompson [68] and are applied in NS-FV zones (due to their very small spatial extent, these are not visible on Figure 20a). For the full LBM simulation, an outlet pressure is specified at the borders of the computational domain and sponge zones are used in order to prevent disturbances from reaching the domain boundaries.

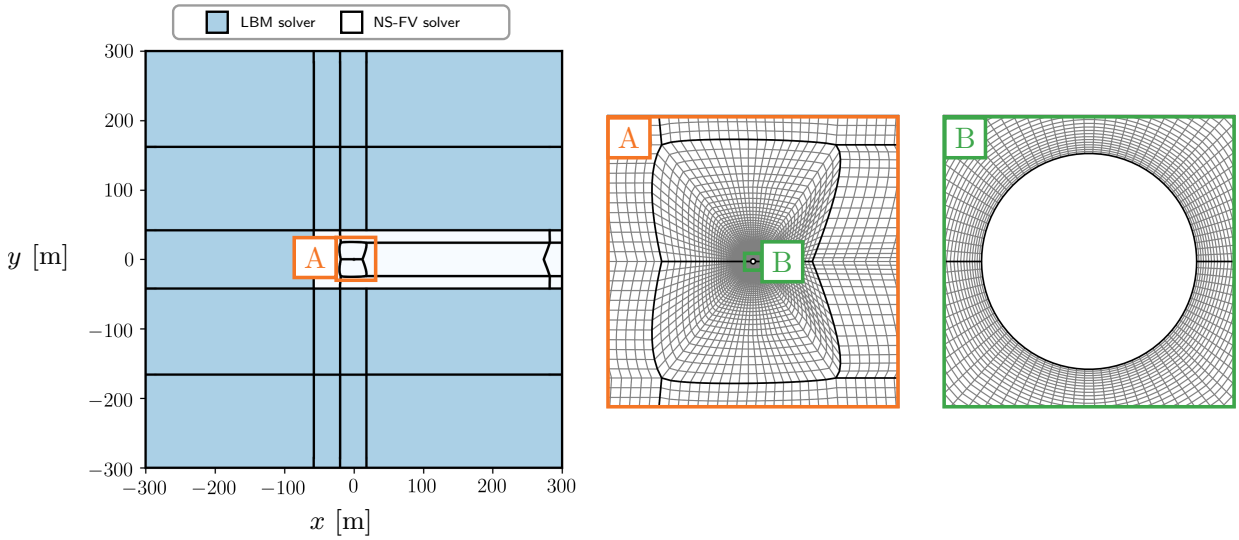

(a) Hybrid lattice Boltzmann - Navier-Stokes and full NS-FV computational grid.

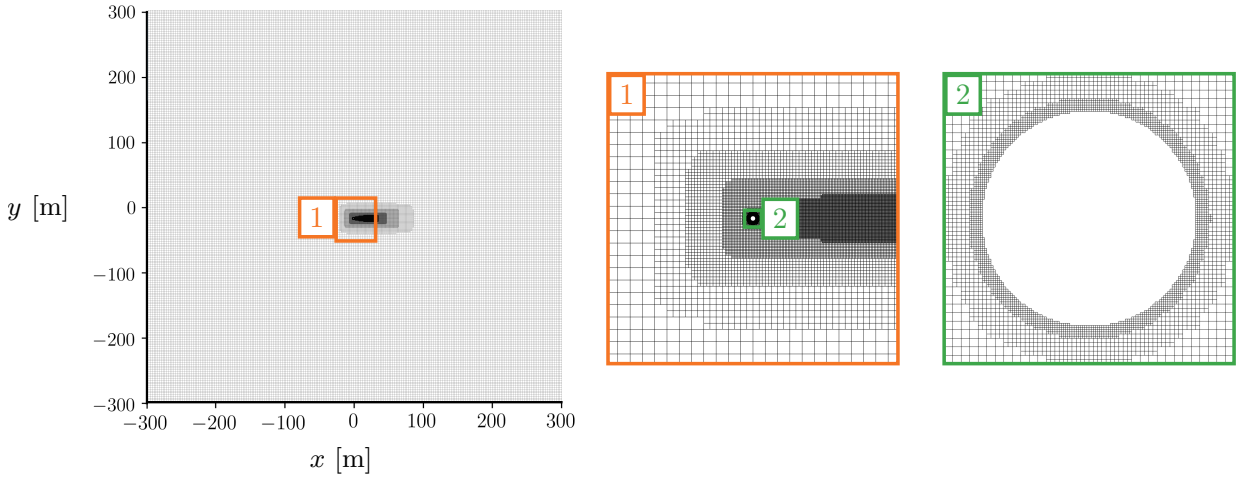

(b) Full LB-HRR computational grid.

Figure 20: Computational domains and associated grids for the aeolian tone radiated by the flow past a circular cylinder. (a) Zonal decomposition for the hybrid lattice Boltzmann - Navier-Stokes method. A total of 48 blocks make up the domain. Moreover, closeups of the hybrid mesh are provided. (b) Cartesian cubic grid used for the full LBM-HRR computation. The mesh was automatically generated by ProLB's octree mesher.

Concerning the grid spacing, special care is taken on the meshes in Figure 20 to ensure that the error

target outlined above is met. In this respect, the first points off the solid surface are placed so as to remain in the boundary layer. Its thickness is estimated by $\delta \approx 1/\sqrt{Re}$ leading to $\delta \approx 0.08$ for $Re = 150$. Consequently, on the cylinder surface, the normal grid size is taken to be $\Delta_n = \delta/10$. While for the mesh in Figure 20a the tangent one can be chosen freely (it is set to $\Delta_s = D/60$ here), the LB mesh forces it to be equal to Δ_n. Conversely, in the acoustic far-field, the mesh size has to be fixed with respect to the wavelength associated to the acoustic radiation λ_{ac}. It can be shown that $\lambda_{\text{ac}} = D/(St \cdot M_\infty)$ where St is the Strouhal number associated to vortex shedding leading to $\lambda_{\text{ac}} \approx 27D$ in the present case. Owing to the low dissipative properties of the lattice Boltzmann method, a number of 14 points per wavelength is chosen (i.e. $\Delta x = \Delta y = \Delta z \approx 2D$) for the full LBM-HRR and hybrid computations. On the other hand, for the full NS-FV computation, a number of 40 points per wavelength is required to capture the correct SPL at a distance of $150D$ off the cylinder. In consequence, the computational domain for the hybrid lattice Boltzmann - Navier-Stokes method is made of about 0.9×10^6 cells, the one for the full LBM-HRR computation contains 1.6×10^6 Equivalent Fine Cells (EFC) while the the full NS-FV one features 8.5×10^6 cells. Both the NS-FV and the hybrid solver use the same time step in the whole computational domain, however, this is not the case for LB computations. Indeed, in the standard LBM the time step depends on the level of refinement, therefore the number of EFCs reflects the workload equivalent of a mesh based only on the minimal mesh size Δx_{min}. Note that a grid convergence study has been performed on the three meshes indicating that these are of minimal size.

As stated earlier, the zonal decomposition for the hybrid lattice Boltzmann - Navier-Stokes computation relies on the distinction between aerodynamic and acoustic regions. Thereby, the Navier-Stokes solver is applied on the body-fitted curvilinear blocks in the vicinity of the cylinder while the lattice Boltzmann solver is devoted to the computation of the far-field acoustics on the Cartesian blocks (see Figure 20a). The NS domain extends throughout the wake zone inasmuch as entropy production cannot be considered as negligible in this flow region and thus the thermodynamic closure of Section 3.2 is no longer valid. Moreover, due to the large disparity in grid sizes, an implicit time-stepping is used by the Navier-Stokes solver to have a physical CFL number of $1/\sqrt{3}$ at both sides of the coupling interface. Therefore, to have a fair comparison, the full Navier-Stokes computation will also be performed by means of an implicit time-stepping scheme.

The use of the hybrid lattice Boltzmann - Navier-Stokes method for such a computation may be very beneficial. Indeed, Figure 20 highlights the fact that the geometry of the cylinder is much more accurately represented with a body-fitted mesh in comparison with the Cartesian "staircase" mesh imposed by standard lattice Boltzmann methods. Even though some authors have proposed solutions to overcome the limit of Cartesian grids for LBMs [69, 70], the exact advection property of the LBM is lost, thereby adding numerical dissipation, and no aeroacoustic studies of such approaches have yet to be published. In addition, one more advantage of the hybrid method can be highlighted. Indeed, mesh-refinement in the lattice Boltzmann

framework may produce spurious noise [62, 71] due to the abrupt non-conformal change of resolution by a factor 2. In the present case, the flexibility of meshing offered by the use of a Navier-Stokes solver enables the use of grid stretching when moving away from the cylinder. Thus, a smooth transition from the near-wall very fine resolution to the acoustic grid size can be achieved.

As in the case of the harmonic acoustic source, one can switch the role of the solvers and still obtain the same quality of solution since the hybrid method is developed so as to provide a two-way coupling. However, in the light of the brief discussion outlined above, switching the role of the solvers might not be of great practical interest since each solver would be in its most unfavourable case.

4.4.1. Aerodynamic study

First, the aerodynamic results of the hybrid method are analysed. At the initial stages of the time evolution, an x-axis symmetric wake composed of two counter-rotating vortices develops downstream of the cylinder. The base flow destabilizes and transitions to an asymmetric von-Karman vortex-street. The alternating vortex shedding from the upper and lower sides of the cylinder is shown in Figure 21 where the instantaneous vorticity field is shown at two distinct instants of time. Consequently, negative and positive pressure pulses are produced alternately from the upper and lower sides of the cylinder, resulting in fluctuating aerodynamic forces.

The parameters of interest are the lift and drag coefficients (denoted by C_l and C_d respectively). These coefficients are defined by:

$$C_l = \frac{F_L}{\frac{1}{2}\rho_\infty u_\infty^2 D} \quad \text{and} \quad C_d = \frac{F_D}{\frac{1}{2}\rho_\infty u_\infty^2 D}. \tag{36}$$

In Equation (36), F_L is the lift force and F_D the drag force. The uniform flow being aligned with the x-axis, the drag corresponds to the horizontal component and the lift force to the vertical component of the total aerodynamic force acting on the cylinder. This force is computed as the sum of two contributions: a locally normal force due to pressure and a friction force due to viscous effects and the no-slip condition. For the sake of completeness, and to assess the quality of the near-wall resolution, the time averaged pressure coefficient C_p is also investigated. It is defined as :

$$C_p = \frac{p_{\text{cyl}} - p_0}{\frac{1}{2}\rho_\infty u_\infty^2}, \tag{37}$$

where p_{cyl} is the local value of pressure on the surface of the cylinder.

Figure 22a, shows the time variations of C_l and C_d for the hybrid, full NS, and full LBM-HRR computations. As stated earlier, the flow around the cylinder is characterised by strong oscillating aerodynamic efforts. The amplitude of the lift coefficient C_l' is much larger than the one of the drag coefficient C_d' suggesting that the associated sound will mainly be due to the lift dipole [66]. The mean value of C_d, denoted by $\overline{C_d}$ hereafter, is 1.378 for both the hybrid and NS computations and 1.41 for the LB simulation. All these values are in agreement with the one obtained by Inoue *et al.* [66], i.e $\overline{C_d} = 1.3805$.

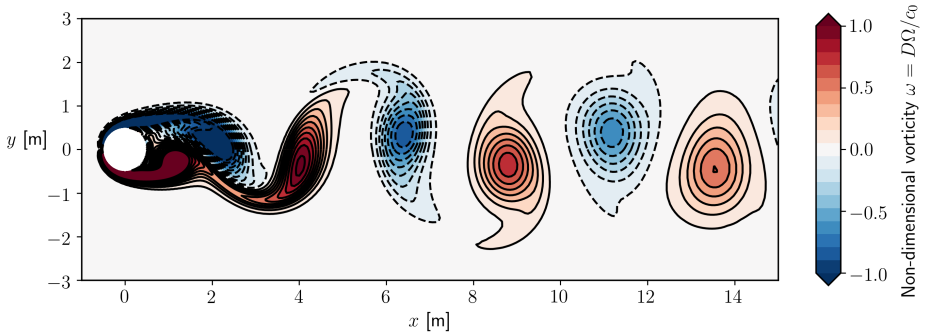

(a)

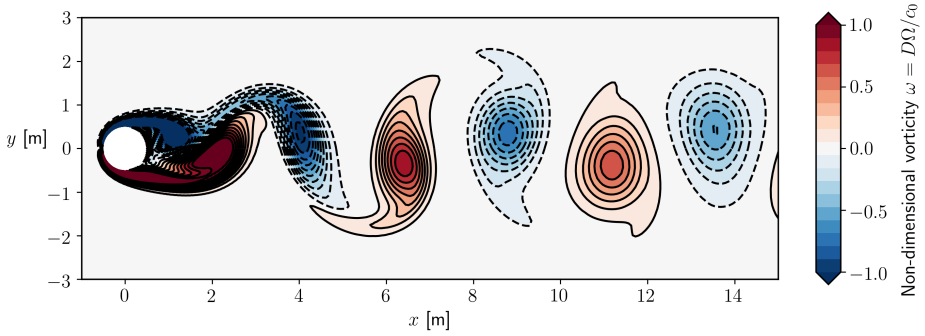

(b)

Figure 21: Time evolution of the non-dimensional vorticity field $\omega = D\Omega/c_0$ where $\Omega = 1/2(\partial_x u_y - \partial_y u_x)$ computed by the hybrid lattice Boltzmann - Navier-Stokes method. (a) Vorticity at the time of minimum C_l and (b) vorticity at the time of maximum C_l. The contour levels are from $\omega_{min} = -1.0$ to $\omega_{max} = 1.0$ with an increment of 0.1. —— : $\omega > 0$ and - - - : $\omega < 0$.

887 The periodic behaviour of both the vortex shedding and the oscillation of the lift coefficient can be
888 described through their characteristic frequency f. Most of the time, this frequency is expressed by means
889 of the non-dimensional Strouhal number $St = fD/U_\infty$. According to Figure 22a, the Strouhal number in
890 the case of the hybrid lattice Boltzmann - Navier-Stokes computation is 0.1817. One can also notice that the
891 drag coefficient C_d is oscillating at twice the frequency of C_l. All the aerodynamic results relative to the lift
892 and drag coefficients are summarised in Table 5 and show good agreement with two reference computations
893 with a Navier-Stokes [66] and lattice-Boltzmann solver [72] respectively. Moreover, as expected, the hybrid
894 method and the full NS computations lead to the same aerodynamic results. In addition, Figure 22b shows
895 the time-averaged pressure coefficient C_p along the cylinder top surface and, regardless of the numerical
896 method, it is in good agreement with the reference DNS of Inoue *et al.* [66].

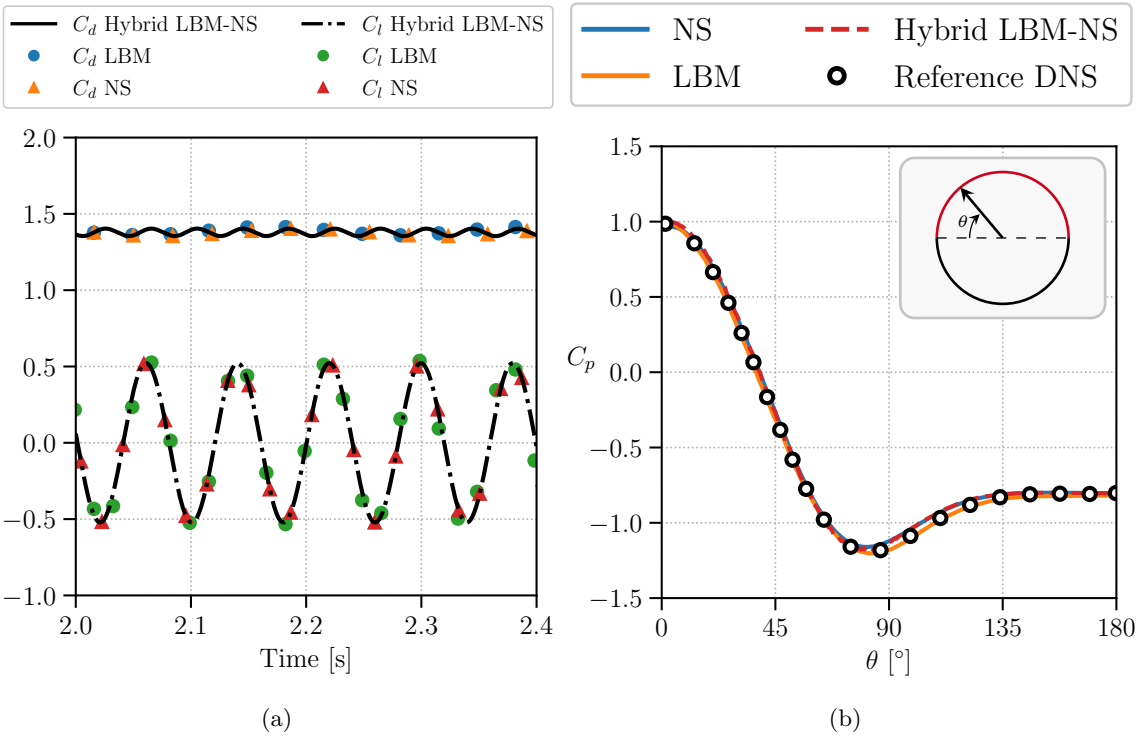

Figure 22: Force coefficients for the flow around a circular cylinder at $M = 0.2$ and $Re = 150$. (a) Time evolution of the lift C_l and drag C_d coefficients. (b) Time-averaged pressure coefficient C_p compared with the reference DNS of Inoue *et al.* [66].

	$\overline{C_d}$	C'_l	C'_d	St
Hybrid LBM-NS	1.378	0.522	0.0248	0.1817
Full NS	1.378	0.522	0.0248	0.1817
Full LBM (ProLB)	1.41	0.537	0.027	0.184
Inoue *et al.* [66]	1.3805	0.52	0.026	0.183
Lafitte *et al.* [72]	1.39	0.56	0.028	0.185

Table 5: Comparison of the characteristic parameters with the Navier-Stokes DNS computation of Inoue *et al.* [66] and a lattice Boltzmann computation by Lafitte *et al.* [72].

4.4.2. Aeroacoustic study

The aerodynamic near-field being validated, the flow induced noise is now analysed. Sound pressure waves are indeed generated by the fluctuating lift force in response to the vortex shedding mechanism. As a consequence, a strong tonal noise at the exact same frequency is expected. In the following, acoustic radiation will be described through the fluctuating pressure field defined (following [66]) as $\Delta\tilde{p}(x, y, t) = \Delta p(x, y, t) - \Delta p_{\text{mean}}(x, y)$. Here $\Delta p = p - p_0$, where p is the total pressure and p_0 its reference value. The effect of the time-averaged fluctuating pressure Δp_{mean} has been extensively discussed in [66].

Figure 23a shows the instantaneous fluctuating pressure field $\Delta\tilde{p}$ in the whole computational domain for the hybrid lattice Boltzmann - Navier-Stokes computation. It can be seen that pressure waves with opposite signs are generated from both upper and lower sides of the cylinder. This indicates the dipolar nature of the radiated acoustic field. Moreover, the pulses propagate radially with time following a propagation angle θ close to its theoretical value $\theta_p = \arccos(M_\infty) = \pm 78.5°$.

In Figure 23b, iso-contours of the instantaneous fluctuating pressure field $\Delta\tilde{p}$ are represented in the vicinity of the coupling interface. The same conclusion as for the previous test cases can be made: the pressure field remains continuous through the interface as no oscillations nor discontinuities in the contour-lines are exhibited. Inasmuch as implicit time-stepping is used by the NS-FV solver, care has been taken to perform enough sub-iterations to fully damp the spurious effect of the explicit boundary treatment. In addition, both plots are symmetrical with respect to the $y = 0$ line and of opposite sign.

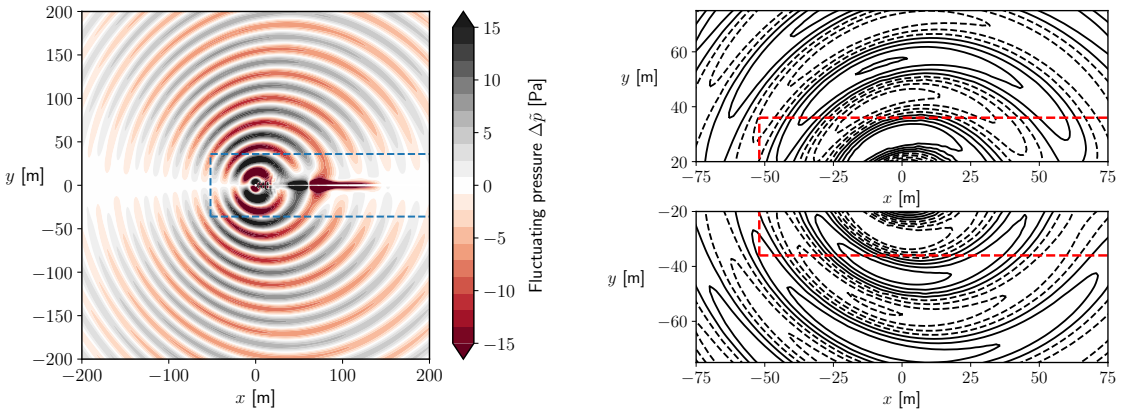

Figure 23: Visualisation of the intantaneous fluctuating pressure field $\Delta\tilde{p}$. (a) Pressure fluctuations in the computational domain between -15 Pa and 15 Pa. The interface between both solvers is indicated by the dashed lines. (b) Iso-contours of pressure fluctuations. The contour levels are from $\Delta\tilde{p}_{min} = -15$ Pa to $\Delta\tilde{p}_{min} = 15$ Pa with an increment of 3.75 Pa. —— : $\Delta\tilde{p} > 0$ and - - - : $\Delta\tilde{p} < 0$.

Inoue *et al.* [66] have shown that the sound radiated by the cylinder is dominated by the lift dipole. The results in Figure 23 tend to verify this conclusion. However, in order to validate more quantitavely the quality of the acoustic field computed with the hybrid lattice Boltzmann - Navier-Stokes method, the polar plot of the root mean square of the fluctuating pressure is studied. The latter quantity is defined as:

$$\Delta p_{\mathrm{rms}}(x,y) = \sqrt{\overline{[\Delta p^2]}(x,y) - [\overline{\Delta p}(x,y)]^2}, \tag{38}$$

where $\overline{[\Delta p^2]}$ is the time average of the squared fluctuating pressure and $\overline{\Delta p}(x,y)$ the time average of the fluctuating pressure. Both values were computed for the last 10 periods of the computation when all the

aerodynamic coefficients reached the statistical steady state.

Figure 24 shows the polar diagram of the root mean square pressure fluctuation Δp_{rms} at a distance of $r = 75D$ and $r = 150D$ of the cylinder for the hybrid, full NS, and full LBM-HRR computations. Note that pressure fluctuations have been made non-dimensional to compare the present results with literature. Indeed, Inoue *et al.* [66] provide a polar plot at $r = 75D$ and, the one at $r = 150D$ is easily obtained by a scaling factor of $\sqrt{75/150}$ to take into account the $r^{-1/2}$ dependence of the amplitude of the sound waves. In each diagram, the radial length from the origin represents the magnitude on a linear scale where the outermost circle corresponds to a value of $\frac{\Delta p_{rms}}{\rho_0 c_0^2} = 1 \times 10^{-4}$ and $\frac{\Delta p_{rms}}{\rho_0 c_0^2} = 0.75 \times 10^{-4}$ respectively.

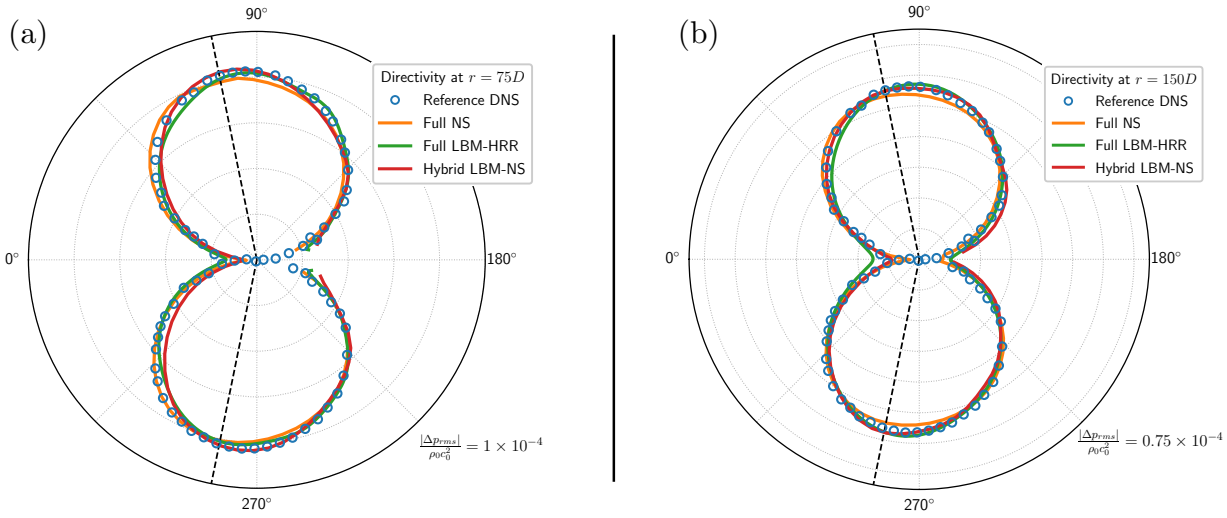

Figure 24: Polar plots of the root mean square of the non-dimensional fluctuating pressure at a distance of (a) $r = 75D$, and (b) $r = 150D$ of the cylinder. The symbols (○) denote the results of the reference computation of Inoue *et al.* [66].

Both plots in Figure 24 confirm the dipolar nature of the sound field. The directivity of the sound waves agrees with its theoretical value of $\theta_p = \pm 78.5°$ due to the Doppler effect as shown by the dashed lines (- - -). All three computations are superimposed to the directivity obtained by the reference DNS [66] thereby further validating the meshes in Figure 20. It is noteworthy that, owing to the low numerical dissipation of the lattice Boltzmann method, the pressure fluctuations can be propagated over long distances with a very limited number of points per wavelength (14 in the present case). Therefore, the hybrid lattice Boltzmann - Navier-Stokes method is very promising when far-field aeroacoustics have to be finely captured.

The last acoustic feature which is studied is the spatial decay of the sound pressure waves. As already stated with the case of the harmonic source of Section 4.3, the pressure peaks tend to decay in proportion to $r^{-1/2}$ with increasing r in two dimensions of space. In order to assess this property in the present case, instantaneous snapshots of the fluctuating pressure $\Delta\tilde{p}$ at four successive instants are plotted against the distance r to the center of the cylinder at $\theta = 90°$ (see Figure 25a). As seen from Figure 25a, pressure waves

propagate radially with time. In addition, the interface between both solvers being shown by the vertical dashed line, it can be confirmed that no reflected waves appear in the vicinity of the coupling interface. To get more insight into the pressure fluctuations decay, the negative and positive peak values of $\Delta\tilde{p}$ are plotted against r in a log-log scale on Figure 25b. A reference line proportional to $r^{-1/2}$ has also been added to this figure. As readily seen from Figure 25b, the pressure peaks computed with the hybrid lattice Boltzmann - Navier-Stokes method tend to decay following a $r^{-1/2}$ slope with increasing r.

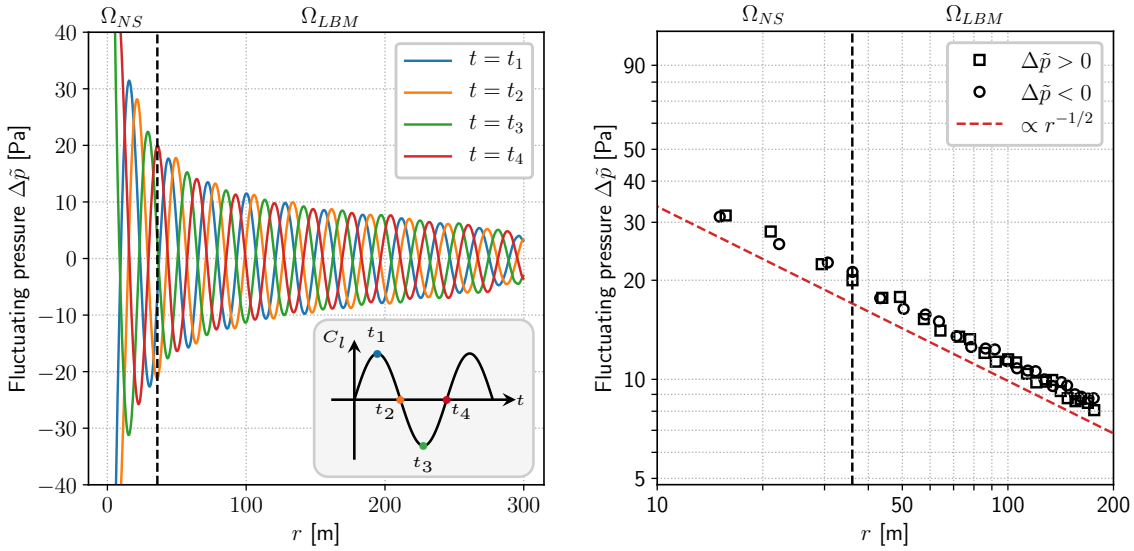

(a) (b)

Figure 25: Propagation and decay of sound waves at $\theta = 90°$. (a) Radial propagation of sound waves with time. 4 differents instants corresponding to specific values of the lift coefficient C_l are chosen to fully describe one period evolution. (b) Decay of both the negative and positive pressure peaks. Comparison with the theoretical decay $\propto r^{-1/2}$.

4.4.3. Computational cost

Some of the advantages of the hybrid lattice Boltzmann - Navier-Stokes method on this specific test case have already been mentioned such as the flexibility on meshing, time-stepping, and the overall accuracy of the approach. The computational cost of the hybrid solver is now investigated. The aim here is not to carry out an in-depth study of the solver's HPC capabilities (in terms of scaling, parallelism, etc.), but rather to give an order of magnitude of the performance, on this specific test case, of both the Navier-Stokes and lattice Boltzmann solvers and to draw some conclusions about the benefits of the hybrid lattice Boltzmann - Navier-Stokes method. All the computations were run on ONERA's development cluster on one bi-socket node consisting of two 12-core Intel Broadwell processors (E5-2650v4, 2.2 GHz) with 128 GB of memory.

First of all, the effective performance of each individual solver of ONERA's CFD suite is studied. While the in-house lattice Boltzmann solver with HRR collision operator achieves 12.6 MCUPS (Million Cells

Update Per Second) per core, the Navier-Stokes solver scales at 3.4 MCUPS per core in the explicit case and at 0.3 MCUPS per core in the implicit case. In comparison, the cost of the hybrid lattice Boltzmann - Navier-Stokes method is not constant since it directly depends on the ratio between NS and LB cells as well as the time-stepping scheme used by the NS solver. For instance, on the mesh in Figure 20, where 25% of the cells are NS ones, the hybrid method reaches 8.9 MCUPS per core when coupled with the NS-implicit solver. These numbers are close to the theoretical value of the performance of the hybrid method:

$$S_{\text{hyb}} = \frac{N_{\text{NS}}}{N_{\text{tot}}} S_{\text{NS}} + \frac{N_{\text{LBM}}}{N_{\text{tot}}} S_{\text{LBM}} \tag{39}$$

where S_{hyb}, S_{NS}, and S_{LBM} are the computational speeds in MCUPS and where $N_{\text{NS}}/N_{\text{tot}}$ and $N_{\text{LBM}}/N_{\text{tot}}$ represent the proportion of cells computed by the NS and the LB solver respectively. As a consequence, one can conclude that the coupling process has a negligible computational footprint.

The three approaches are now compared in terms of CPU efficiency. As stated earlier, the metric of interest is the total CPU time $T^{5\%}_{\text{CPU}}$ required to capture both the sound pressure level (SPL) at a distance of $r = 150D$ of the cylinder and the correct boundary layer (in terms of C_l, C_d and C_p) within a 5% error-margin with respect to their theoretical values. The results are summarised in Table 6 where $T^{5\%}_{\text{CPU}}$ is provided for the hybrid LBM-NS, full NS, and full LBM-HRR computations respectively. Note that the total CPU time only takes into account the effective time of computation and does not include the time needed for the evaluation of post-processing quantities such as statistics. Moreover, to ease the comparison, the relative cost of each method with respect to the hybrid approach and the total number of cells in the computational grid are also reported.

It should be noted that the computational time indicated in Table 6 for the full LBM-HRR computation is an estimated one. As a matter of fact, the ProLB solver which is used for the aerodynamic and aeroacoustic studies (see Sections 4.4.1 and 4.4.2) is an unstructured one, thus its computational time is not representative of the performance which can be achieved by using the in-house LB solver. In addition, the comparison of the CPU time obtained with ProLB with the hybrid method would be unfair since the latter is using ONERA's in-house structured lattice Boltzmann software. Thereby, the value of $T^{5\%}_{\text{CPU}}$ provided in Table 6 for a full LBM-HRR simulation was computed by dividing the number of EFC by the performance in MCUPS of ONERA's LB solver to reach converged statistics.

From Table 6, one can easily see that the hybrid lattice Boltzmann - Navier-Stokes methods is the most efficient one to reproduce both the aerodynamics and the acoustics within the targeted error range. Indeed, due to the high dissipation of acoustic modes by full Navier-Stokes computations, the number of mesh points per wavelength has to be increased in the acoustic region leading to a 10-fold increase in the number of cells in the computational grid with respect to the mesh of the hybrid method. Hence, for the same level of accuracy, the hybrid lattice Boltzmann - Navier-Stokes method is about 2.7 times faster than a full NS-FV

	N_{cells} [M]	Δt [s]	$T^{5\%}_{\text{CPU}}$ [s]	$T^{5\%}_{\text{CPU}} / \left(T^{5\%}_{\text{CPU}}\right)_{\text{hyb}}$
Hybrid LBM-NS	0.91	3.3×10^{-3}	3877	1
Full LBM-HRR†	1.6 (EFC)	1.7×10^{-5}	7893	2.04
Full NS-Implicit	8.5	1.2×10^{-2}	10 442	2.69

Table 6: Comparison of the computational costs of the hybrid lattice Boltzmann method with full NS-FV and full LB computations to capture both the correct SPL at a distance of $r = 150D$ of the source and the correct boundary layer within a 5% error-margin w.r.t their theoretical values. †: The total CPU time $T^{5\%}_{\text{CPU}}$ for the LBM computation is an estimated one.

implicit computation. This clearly shows the advantage of using the LBM as an acoustic propagator.

Conversely, to highlight the benefit of using the NS-FV solver in the near-wall region, the computational cost of the hybrid method is compared to a full LBM-HRR computation. As shown in Table 6, a full LBM-HRR computation is about 2 times slower than the one performed with the hybrid lattice Boltzmann - Navier-Stokes method. This increase in computational time is mainly explained by the fact that wall-resolved computations are expensive within the LB framework since the method is restricted to cubic cells $\Delta x = \Delta y = \Delta z$ and evolving with an explicit time-stepping scheme at a fixed CFL number. To give an order of magnitude, about 95% of the cells in the full LB mesh (1.5×10^6 cells) are located within the cylinder's near wake region. In contrast, for the hybrid lattice Boltzmann - Navier-Stokes mesh, only 12% of the cells (0.1×10^6 cells) make up this flow region. Moreover, this value of $T^{5\%}_{\text{CPU}}$ is just a lower bound estimate since it does not take into account any specific algorithmic treatment at the interface between the resolution domains. This clearly shows the advantage of using the NS-FV solver in the near-wall region when the levels of accuracy provided by wall functions in insufficient thereby justifying the need of wall resolved computations.

This short discussion on computational costs helps to underline one more benefit of the hybrid method. Since each numerical method is the most efficient in different regions of the flow, combining them spatially and temporally can reduce the CPU time needed to compute multi-physics problems. Note that the hybrid method could be even more efficient by using explicit local time stepping [73]. Indeed, as most of the time computational time spend in evolving the NS-FV implicit domains, removing the implicit time stepping might lead to another increase in terms of CPU efficiency. This is planned for future work.

5. Conclusions

In this paper, a hybrid lattice Boltzmann - Navier-Stokes method for unsteady aerodynamic and aeroacoustic simulations has been proposed. This method relies on the partitioning of the computational domain into distinct non-overlapping regions where either the lattice Boltzmann or a compressible finite-volume Navier-Stokes method is applied. The technical difficulties of a two-way coupling between both solvers have

been discussed and it has been shown that such procedure is not straightforward as each numerical methods relies on its own set of variables. The heart of the coupling methodology lies on the way the LB distribution functions are obtained from macroscopic flow quantities and their derivatives. In the present study, the distribution functions are obtained through a first-order Chapman-Enskog expansion without any prior approximation on their expressions. One of the original features of this strategy is the direct link which has been drawn between the reconstruction procedure and the HRR collision operator. Moreover, special care is taken when coupling various time-stepping schemes with the lattice Boltzmann stream and collide algorithm. A detailed evaluation of time-interpolation methods is therefore performed in the context of computational aeroacoustics.

The hybrid lattice Boltzmann - Navier-Stokes method is assessed on four benchmark cases. While the gaussian 1D acoustic wave shows the influence of each component of the coupling procedure, the convection of a barotropic vortex demonstrates the feasibility of the proposed approach in an unsteady context and shows a second order convergence of the hybrid method in both space and time. The acoustic radiation of a harmonic source and the flow past a circular cylinder help to demonstrate the benefits and capabilities of the the hybrid method. Firstly, the low dissipation of the lattice Boltzmann method allows to reduce the number of mesh points per wavelength in acoustic regions and thereby the total size of computational grids. Secondly, when computing the flow around obstacles, the use of the Navier-Stokes method in near-wall regions enables to accurately describe complex geometries through the use of body-fitted meshes. Hence, complex flow phenomena are directly resolved and no wall laws are needed as is commonly the case in the lattice Boltzmann framework. Thirdly, and most importantly, the overall computational cost is reduced by the use of the hybrid approach for simulations where both the aerodynamics and acoustics are computed simultaneously. When considering the aeolian tone of the flow past a circular cylinder, using the coupled solver helps to decrease the total CPU time by a factor two with respect to full Navier-Stokes and lattice Boltzmann computations. To the authors knowledge, the present hybrid lattice Boltzmann - Navier-Stokes method is the first one being introduced and validated in the context of aeroacoustic computations.

Future work will consist in extending the strategy to more complex interface geometries such as mesh refinements and non-conforming grids. It is also believed that the lattice Boltzmann method could be an interesting candidate for the propagation of turbulent wakes over long distances. Therefore, temperature fluctuations and compressibility effects have to be accounted for in the lattice Boltzmann solver or at least at the interface. In addition, exploring other time stepping strategies might help to improve the overall computational cost of the hybrid solver. As a perspective, it would then be interesting to evaluate the hybrid lattice Boltzmann - Navier-Stokes method on representative aeronautical applications, such as cavity or trailing edge noise, where both the boundary layer and the acoustics have to be accurately characterised.

Acknowledgements

The authors are grateful to Antoine Michael Diego Jost for the final proofreading of this article.

Appendix A. Mixed Taylor/Chapman-Enskog expansion

In this appendix, the mixed Taylor/Chapman-Enskog expansion of the lattice Boltzmann scheme is detailed. Therefore, Equation (11) is written in a slightly different way by introducing the time-step Δt and by recasting the regularised collision operator in a BGK-like fashion:

$$g_i(\boldsymbol{x}+\boldsymbol{\xi}_i\Delta t, t+\Delta t) = g_i(\boldsymbol{x},t) - \frac{\Delta t}{\overline{\tau}}\left(g_i(\boldsymbol{x},t) - g_i^{eq}(\boldsymbol{x},t)\right) + \frac{\Delta t}{2}\psi_i(\boldsymbol{x},t). \tag{A.1}$$

Assuming that the time step Δt is small, a second-order Taylor-expansion is performed on the left hand-side of equation (A.1) yielding:

$$\Delta t\left[\frac{\partial}{\partial t} + \boldsymbol{\xi}_i\frac{\partial}{\partial \boldsymbol{x}}\right] g_i + \frac{\Delta t^2}{2}\left[\frac{\partial}{\partial t} + \boldsymbol{\xi}_i\frac{\partial}{\partial \boldsymbol{x}}\right]^2 g_i = -\frac{\Delta t}{\overline{\tau}}\left(g_i - g_i^{eq}\right) + \frac{\Delta t}{2}\psi_i + \mathcal{O}(\Delta t^3), \tag{A.2}$$

where the explicit space and time dependance of the distribution functions and of the corrective term has been dropped for the sake of clarity. The second-order derivative term appearing in equation (A.2) has often been neglected without any rigorous explanation [15, 18]. In fact, it can be discarded by subtracting $(\Delta t/2)(\partial_t + \boldsymbol{\xi}_i\partial_{\boldsymbol{x}})$ applied to the equation itself. Dividing the final equation by Δt, one obtains:

$$\left[\frac{\partial}{\partial t} + \boldsymbol{\xi}_i\frac{\partial}{\partial \boldsymbol{x}}\right] g_i = -\frac{1}{\overline{\tau}}g_i^{neq} + \frac{1}{2}\psi_i + \frac{\Delta t}{2\overline{\tau}}\left[\frac{\partial}{\partial t} + \boldsymbol{\xi}_i\frac{\partial}{\partial \boldsymbol{x}}\right] g_i^{neq} + \frac{\Delta t}{2}\left[\frac{\partial}{\partial t} + \boldsymbol{\xi}_i\frac{\partial}{\partial \boldsymbol{x}}\right]\psi_i + \mathcal{O}(\Delta t^2), \tag{A.3}$$

where $g_i^{neq} = g_i - g_i^{eq}$. At this stage, a first relation defining the off-equilibrium distribution functions is obtained. Nevertheless, the aim is to express this off-equilibrium term as a function of the macroscopic variables. Therefore, a Chapman-Enskog expansion [74] is now performed.

The Chapman-Enskog expansion [74] is a mathematical tool commonly used to understand the link between the Boltzmann equation and the macroscopic Navier-Stokes equations. The formalism, which has been developed in the continuous case, consists in expanding the space- and time-continuous distribution functions f_i in powers of a small parameter ϵ which can be identified to the Knudsen number Kn:

$$f_i\left[\rho(\boldsymbol{x},t), \rho\boldsymbol{u}(\boldsymbol{x},t)\right] = \sum_{n=0}^{\infty}\epsilon^n f_i^{(n)}\left[\rho(\boldsymbol{x},t), \rho\boldsymbol{u}(\boldsymbol{x},t)\right]. \tag{A.4}$$

The expansion parameter ϵ indicates that $f_i^{(1)}/f_i^{(0)} = \mathcal{O}(\mathrm{Kn})$, $f_i^{(2)}/f_i^{(0)} = \mathcal{O}(\mathrm{Kn}^2)$ and so on. Moreover, as any collision operator must conserve mass and momentum, the following conditions are imposed on the high-order terms of the expansion:

$$\sum_{i=1}^{q} f_i^{(k)} = 0 \quad \text{and} \quad \sum_{i=1}^{q}\boldsymbol{\xi}_i f_i^{(k)} = \boldsymbol{0} \quad \text{for } k \geq 1. \tag{A.5}$$

These conditions are also called the solvability conditions. Mathematically, they represent the search for normal solutions of the Boltzmann equation.

Besides the expansion of the space- and time-continuous distribution functions f_i, the time and space derivative operators are also expanded in terms of ϵ:

$$\frac{\partial}{\partial t} = \epsilon \frac{\partial}{\partial t_1} + \epsilon^2 \frac{\partial}{\partial t_2} \quad \text{and} \quad \frac{\partial}{\partial \boldsymbol{x}} = \epsilon \frac{\partial}{\partial \boldsymbol{x}_1}. \tag{A.6}$$

The time derivative is expressed as the sum of a fast convective time scale t_1 and a slow diffusive time scale t_2 whereas the space derivative is expanded to the first order as only the large scale dynamics are of interest.

The expansion introduced in Equation (A.4) can not be applied as is on Equation (A.3) owing to the variable change performed when discretising the DVBE in both space and time. Indeed, in the case of the corrected HRR collision operator, the space- and time-discrete distribution functions g_i are defined as:

$$g_i = f_i + \frac{\Delta t}{2\tau}(f_i - f_i^{eq}) - \frac{\Delta t}{2}\psi_i. \tag{A.7}$$

By combining Equation (A.4) and Equation (A.7), the following expansion is obtained:

$$g_i = \sum_{n=0}^{\infty} \epsilon^n f_i^{(n)} + \frac{\Delta t}{2\tau}\left(\sum_{n=0}^{\infty} \epsilon^n f_i^{(n)} - f_i^{eq}\right) - \frac{\Delta t}{2}\epsilon\psi_i^{(1)}, \tag{A.8}$$

where the corrective term ψ_i has been expanded to the first order. In addition, it can also be shown that:

$$g_i^{neq} = g_i - g_i^{eq} = \left(1 + \frac{\Delta t}{2\tau}\right)\left(\sum_{n=0}^{\infty} \epsilon^n f_i^{(n)} - f_i^{eq}\right) = \frac{\overline{\tau}}{\tau}\left(\sum_{n=0}^{\infty} \epsilon^n f_i^{(n)} - f_i^{eq}\right). \tag{A.9}$$

Substituting Equations (A.6), (A.8) and (A.9) into Equation (A.3), the resulting equation can be separated according to the different orders of ϵ leading to an infinite set of cascaded equations. The target equations being here the Navier-Stokes equations, a first order Chapman-Enskog expansion in ϵ is sufficient [74]. Therefore, by keeping only the first two equations (i.e. the ones corresponding to $\mathcal{O}(\epsilon^0)$ and $\mathcal{O}(\epsilon)$), the following relations are deduced:

$$0 = -\frac{1}{\tau}\left(f_i^{(0)} - f_i^{eq}\right) + \mathcal{O}(\Delta t^2), \tag{A.10}$$

and,

$$\left(\left[\frac{\partial}{\partial t_1} + \boldsymbol{\xi}_i \frac{\partial}{\partial \boldsymbol{x}_1}\right] f_i^{(0)} - \psi_i\right) = -\frac{1}{\tau} f_i^{(1)} + \mathcal{O}(\Delta t^2). \tag{A.11}$$

In the following, the first-order approximation of the off-equilibrium part of the distribution functions given by Equation (A.11) will be denoted by $f_i^{neq,(1)}$.

Appendix B. Reconstructed off-equilibrium contribution in the case of the HRR-LBM

Malaspinas derived in [49] an elegant recursive relation for the off-equilibrium moments in the context of the athermal Boltzmann-BGK equation. In this Appendix, it is proposed to use the same formalism in order

to show that the reconstructed off-equilibrium component in the hybrid lattice Boltzmann - Navier-Stokes method is genuinely contained in the HRR lattice Boltzmann scheme.

As introduced in Section 2.2.2, both the equilibrium and the off-equilibrium distribution functions of the bulk lattice Boltzmann solver are expanded using the Hermite formalism. Therefore, to ensure consistency, one can expand f_i^{eq} and $f_i^{neq,(1)}$ appearing in Equation (21) in the same way, such as:

$$f_i^{eq} = w_i \sum_{n=0}^{N} \frac{1}{c_s^{2n} n!} \boldsymbol{a}_0^{(n)} : \boldsymbol{\mathcal{H}}_i^{(n)} \quad \text{and} \quad f_i^{neq,(1)} = w_i \sum_{n=0}^{N_r} \frac{1}{c_s^{2n} n!} \boldsymbol{a}_1^{(n)} : \boldsymbol{\mathcal{H}}_i^{(n)}, \tag{B.1}$$

In Equation (B.1), $\boldsymbol{a}_0^{(n)}$ and $\boldsymbol{a}_1^{(n)}$ are the equilibrium and off-equilibrium Hermite coefficients defined as:

$$\boldsymbol{a}_0^{(n)} = \sum_{i=1}^{q} f_i^{eq} \boldsymbol{\mathcal{H}}_i^{(n)} \quad \text{and} \quad \boldsymbol{a}_1^{(n)} = \sum_{i=1}^{q} f_i^{neq,(1)} \boldsymbol{\mathcal{H}}_i^{(n)}. \tag{B.2}$$

By projecting Equation (21) onto the basis of Hermite polynomials and using Rodrigues' formula [75], it simplifies into:

$$\frac{\partial}{\partial t} a_{0,\alpha_1 \dots \alpha_n}^{(n)} + \frac{\partial}{\partial \alpha_{n+1}} a_{0,\alpha_1 \dots \alpha_n \alpha_{n+1}}^{(n+1)} + c_s^2 \sum_{i=1}^{n} \frac{\partial}{\partial \alpha_i} a_{0,\overline{\alpha_i}}^{(n-1)} + \delta_{2n} a_{\psi,\alpha_1 \alpha_2}^{(2)} = -\frac{1}{\tau} a_{1,\alpha_1 \dots \alpha_n}^{(n)}, \tag{B.3}$$

where the notation $\overline{\alpha_i} = \alpha_1 ... \alpha_{i-1} \alpha_{i+1} ... \alpha_n$ has been introduced for the sake of clarity. Equation (B.3) is almost the same as the one derived in [49] except it exhibits a contribution due to the corrective term ψ_i through $a_{\psi,\alpha_1\alpha_2}^{(2)}$. The most interesting point about this term is that it only contributes to Equation (B.3) when $n = 2$. Indeed, as shown by Equation (12), the corrective term is defined with 2nd-order Hermite polynomials. Yet, by virtue of the orthogonality properties of Hermite polynomials [75], one directly has $a_{\psi,\alpha_1 \dots \alpha_n}^{(n)} = 0$ if $n \neq 2$ which justifies the use of the Kronecker delta δ_{2n} as a prefactor.

After some algebra (we refer the reader to [49] for the calculation steps), this relation can be further simplified as:

$$a_{1,\alpha_1 \dots \alpha_n}^{(n)} = u_{\alpha_n} a_{1,\alpha_1 \dots \alpha_{n-1}}^{(n-1)} + \sum_{i=1}^{n-1} u_{\alpha_1} ... u_{\alpha_{n-2}} a_{1,\alpha_i \alpha_n}^{(2)} \quad \text{for } n \geq 3. \tag{B.4}$$

Again, as for Equation (B.3), the resulting recursive relation is almost the same as the one derived in [49]. However, this time, the difference is implicit as it occurs in the definition of $\boldsymbol{a}_1^{(2)}$ which constitutes the initialisation step of the recursive formula. Indeed, in [49] the Hermite coefficient $\boldsymbol{a}_1^{(2)}$ was computed thanks to a Chapman-Enskog expansion leading to $a_1^{(2)} = -2\rho\tau c_s^2 \mathbf{S} + \mathcal{O}(\mathrm{Ma}^3)$ where $\mathbf{S} = \frac{1}{2}\left(\nabla \boldsymbol{u} + \nabla \boldsymbol{u}^T\right)$. The cubic Mach error term (which does not appear in the Navier-Stokes equations) was then neglected thanks to a low Mach number approximation. However, in the present case, the ψ_i corrective term is specifically designed such as to remove the cubic Mach error term. Therefore, after a Chapman-Enskog expansion one exactly obtains $a_1^{(2)} = -2\rho\tau c_s^2 \mathbf{S}$ which means that all the quadrature-related error terms are properly discarded and that no approximation regarding the Mach number has to be made.

References

[1] A. Abbas-Bayoumi, K. Becker, An industrial view on numerical simulation for aircraft aerodynamic design, Journal of Mathematics in Industry 1 (2011) 1–14. doi:10.1186/2190-5983-1-10.

[2] R. Löhner, Towards overcoming the LES crisis, International Journal of Computational Fluid Dynamics 33 (3) (2019) 87–97. doi:10.1080/10618562.2019.1612052.

[3] P. Sagaut, S. Deck, Large eddy simulation for aerodynamics: status and perspectives, Philosophical Transactions of the Royal Society A: Mathematical, Physical and Engineering Sciences 367 (2009) 2849–2860. doi:10.1098/RSTA.2008.0269.

[4] Y. H. Qian, D. D'Humières, P. Lallemand, Lattice BGK Models for Navier-Stokes Equation, Europhysics Letter 17 (6) (1992) 479–484. doi:10.1209/0295-5075/17/6/001.

[5] S. Chen, G. D. Doolen, Lattice Boltzmann method for fluid flows, Annual Review of Fluid Mechanics 30 (1) (1998) 329–364. doi:10.1146/annurev.fluid.30.1.329.

[6] P. Lallemand, L.-S. Luo, M. Krafczyk, W.-A. Yong, The Lattice Boltzmann Method for Nearly Incompressible Flows, Journal of Computational Physicsdoi:10.1016/j.jcp.2020.109713.

[7] S. Marié, D. Ricot, P. Sagaut, Comparison between lattice Boltzmann method and Navier-Stokes high order schemes for computational aeroacoustics, Journal of Computational Physics 228 (4) (2009) 1056–1070. doi:10.1016/j.jcp.2008.10.021.

[8] Y. Hou, D. Angland, A. Sengissen, A. Scotto, lattice-Boltzmann and Navier-Stokes simulations of the partially dressed, cavity-closed nose landing gear benchmark case, in: 25th AIAA/CEAS Aeroacoustics Conference, 2019, American Institute of Aeronautics and Astronautics Inc, AIAA, 2019. doi:10.2514/6.2019-2555.

[9] M. Daroukh, T. L. Garrec, C. Polacsek, Low-Speed Turbofan Aerodynamic and Acoustic Prediction with an Isothermal Lattice Boltzmann Method, AIAA Journaldoi:10.2514/1.J060752.

[10] M. R. Khorrami, E. Fares, Toward noise certification during design: airframe noise simulations for full-scale, complete aircraft, CEAS Aeronautical Journal 10 (1) (2019) 31–67. doi:10.1007/s13272-019-00378-1.

[11] U. Piomelli, Wall-layer models for large-eddy simulations, Progress in Aerospace Sciences 44 (6) (2008) 437–446. doi:10.1016/j.paerosci.2008.06.001.

[12] Z. X. Tong, Y. L. He, W. Q. Tao, A review of current progress in multiscale simulations for fluid flow and heat transfer problems: The frameworks, coupling techniques and future perspectives, International Journal of Heat and Mass Transfer 137 (2019) 1263–1289. doi:10.1016/J.IJHEATMASSTRANSFER.2019.04.004.

[13] J. Latt, B. Chopard, P. Albuquerque, Spatial Coupling of a Lattice Boltzmann fluid model with a Finite Difference Navier-Stokes solverarXiv:0511243.

[14] P. Albuquerque, D. Alemani, B. Chopard, P. Leone, A hybrid lattice Boltzmann finite difference scheme for the diffusion equation, International Journal for Multiscale Computational Engineering 4 (2) (2006) 209–219. doi:10.1615/intjmultcompeng.v4.i2.20.

[15] H. B. Luan, H. Xu, L. Chen, D. L. Sun, W. Q. Tao, Numerical illustrations of the coupling between the lattice boltzmann method and finite-type macro-numerical methods, Numerical Heat Transfer, Part B: Fundamentals 57 (2) (2010) 147–171. doi:10.1080/15421400903579929.

[16] H. Xu, H. Luan, Y. He, W. Tao, A lifting relation from macroscopic variables to mesoscopic variables in lattice Boltzmann method: Derivation, numerical assessments and coupling computations validation, Computers and Fluids 54 (1) (2012) 92–104. doi:10.1016/j.compfluid.2011.10.007.

[17] H. B. Luan, H. Xu, L. Chen, D. L. Sun, Y. L. He, W. Q. Tao, Evaluation of the coupling scheme of FVM and LBM for fluid flows around complex geometries, International Journal of Heat and Mass Transfer 54 (9-10) (2011) 1975–1985. doi:10.1016/J.IJHEATMASSTRANSFER.2011.01.004.

[18] Z. X. Tong, Y. L. He, A unified coupling scheme between lattice Boltzmann method and finite volume method for

unsteady fluid flow and heat transfer, International Journal of Heat and Mass Transfer 80 (2015) 812–824. doi:10.1016/J.IJHEATMASSTRANSFER.2014.09.067.

[19] P. Neumann, H. J. Bungartz, M. Mehl, T. Neckel, T. Weinzierl, A coupled approach for fluid dynamic problems using the PDE framework Peano, Communications in Computational Physics 12 (1) (2012) 65–84. doi:10.4208/cicp.210910.200611a.

[20] A. Atanasov, B. Uekermann, C. Pachajoa Mejía, H.-J. Bungartz, P. Neumann, Steady-State Anderson Accelerated Coupling of lattice Boltzmann and Navier–Stokes Solvers, Computation 4 (4) (2016) 38. doi:10.3390/computation4040038.

[21] P. Neumann, On transient hybrid lattice Boltzmann–Navier-Stokes flow simulations, Journal of Computational Science 17 (2016) 482–490. doi:https://doi.org/10.1016/j.jocs.2016.02.003.

[22] J. Jacob, O. Malaspinas, P. Sagaut, A new hybrid recursive regularised Bhatnagar–Gross–Krook collision model for lattice Boltzmann method-based large eddy simulation, Journal of Turbulence 19 (11) (2019) 1051–1076. doi:10.1080/14685248.2018.1540879.

[23] https://w3.onera.fr/FAST/.

[24] C. Benoit, S. Péron, S. Landier, Cassiopee: A CFD pre- and post-processing tool, Aerospace Science and Technology 45 (2015) 272–283. doi:10.1016/j.ast.2015.05.023.

[25] I. Mary, P. Sagaut, Large eddy simulation of flow around an airfoil near stall, AIAA Journal 40 (6) (2002) 1139–1145. doi:10.2514/2.1763.

[26] J. R. Edwards, M. S. Liou, Low-diffusion flux-splitting methods for flows at all speeds, AIAA Journal 36 (9) (1998) 1610–1617. doi:10.2514/2.587.

[27] P. S. Lowery, W. C. Reynolds, Numerical simulation of a spatially-developping, forced, plane mixing layer, Tech. Rep. TF26, Stanford University (1986).

[28] F. Daude, I. Mary, P. Comte, Self-Adaptive Newton-based iteration strategy for the LES of turbulent multi-scale flows, Computers & Fluids 100 (2014) 278–290. doi:10.1016/J.COMPFLUID.2014.04.028.

[29] A. Jameson, S. Yoon, Lower-upper implicit schemes with multiple grids for the Euler equations, AIAA Journal 25 (7) (1987) 929–935. doi:10.2514/3.9724.

[30] T. J. Coakley, Implicit upwind methods for the compressible Navier-Stokes equations, AIAA Journal 23 (3) (1985) 374–380. doi:10.2514/3.8923.

[31] L. Célia, I. Mary, V. Gleize, A. Lerat, D. Arnal, DNS database of a transitional separation bubble on a flat plate and application to RANS modeling validation, Computers & Fluids 61 (2012) 21–30. doi:10.1016/J.COMPFLUID.2011.07.011.

[32] N. Alferez, I. Mary, E. Lamballais, Study of Stall Development Around an Airfoil by Means of High Fidelity Large Eddy Simulation, Flow, Turbulence and Combustion 2013 91:3 91 (3) (2013) 623–641. doi:10.1007/S10494-013-9483-7.

[33] J. Dandois, I. Mary, V. Brion, Large-eddy simulation of laminar transonic buffet, Journal of Fluid Mechanics 850 (2018) 156–178. doi:10.1017/JFM.2018.470.

[34] S. Péron, C. Benoit, T. Renaud, I. Mary, An immersed boundary method on Cartesian adaptive grids for the simulation of compressible flows around arbitrary geometries, Engineering with Computers 1 (2020) 3. doi:10.1007/s00366-020-00950-y.

[35] P. L. Bhatnagar, E. P. Gross, M. Krook, A model for collision processes in gases. I. Small amplitude processes in charged and neutral one-component systems, Physical Review 94 (3) (1954) 511–525. doi:10.1103/PhysRev.94.511.

[36] X. He, L. S. Luo, Theory of the lattice Boltzmann method: From the Boltzmann equation to the lattice Boltzmann equation, Physical Review E - Statistical Physics, Plasmas, Fluids, and Related Interdisciplinary Topics 55 (6) (1997) 6811–6820. doi:10.1103/PhysRevE.56.6811.

[37] X. Shan, X. F. Yuan, H. Chen, Kinetic theory representation of hydrodynamics: A way beyond the Navier-Stokes equation, Journal of Fluid Mechanics 550 (2006) 413–441. doi:10.1017/S0022112005008153.

[38] P. J. Dellar, Bulk and shear viscosities in lattice Boltzmann equations, Physical Review E - Statistical Physics, Plasmas, Fluids, and Related Interdisciplinary Topics 64 (3) (2001) 11. doi:10.1103/PhysRevE.64.031203.

[39] X. He, S. Chen, G. D. Doolen, A Novel Thermal Model for the Lattice Boltzmann Method in Incompressible Limit, Journal of Computational Physics 146 (1) (1998) 282–300. doi:10.1006/jcph.1998.6057.

[40] P. J. Dellar, An interpretation and derivation of the lattice Boltzmann method using Strang splitting, Computers & Mathematics with Applications 65 (2) (2013) 129–141. doi:10.1016/j.camwa.2011.08.047.

[41] P. Lallemand, L. S. Luo, Theory of the lattice Boltzmann method: Dispersion, dissipation, isotropy, Galilean invariance, and stability, Physical Review E - Statistical Physics, Plasmas, Fluids, and Related Interdisciplinary Topics 61 (6) (2000) 6546–6562. doi:10.1103/PhysRevE.61.6546.

[42] P. J. Dellar, Nonhydrodynamic modes and a priori construction of shallow water lattice Boltzmann equations, Physical Review E - Statistical Physics, Plasmas, Fluids, and Related Interdisciplinary Topics 65 (3) (2002) 036309. doi:10.1103/PhysRevE.65.036309.

[43] P. Lallemand, L. S. Luo, Theory of the lattice Boltzmann method: Acoustic and thermal properties in two and three dimensions, Physical Review E 68 (3) (2003) 036706. doi:10.1103/PhysRevE.68.036706.

[44] G. Wissocq, P. Sagaut, J.-F. Boussuge, An extended spectral analysis of the lattice Boltzmann method: modal interactions and stability issues, Journal of Computational Physics 380 (2019) 311–333. doi:10.1016/j.jcp.2018.12.015.

[45] D. D'Humières, I. Ginzburg, M. Krafczyk, P. Lallemand, L. S. Luo, Multiple-relaxation-time lattice Boltzmann models in three dimensions, in: Philosophical Transactions of the Royal Society A: Mathematical, Physical and Engineering Sciences, Vol. 360, Philos Trans A Math Phys Eng Sci, 2002, pp. 437–451. doi:10.1098/rsta.2001.0955.

[46] M. Geier, M. Schönherr, A. Pasquali, M. Krafczyk, The cumulant lattice Boltzmann equation in three dimensions: Theory and validation, Computers & Mathematics with Applications 70 (4) (2015) 507–547. doi:https://doi.org/10.1016/j.camwa.2015.05.001.

[47] N. Frapolli, S. S. Chikatamarla, I. V. Karlin, Entropic lattice Boltzmann model for gas dynamics: Theory, boundary conditions, and implementation, Physical Review E 93 (6) (2016) 063302. doi:10.1103/PhysRevE.93.063302.

[48] J. Latt, B. Chopard, Lattice Boltzmann method with regularized pre-collision distribution functions, Mathematics and Computers in Simulation 72 (2) (2006) 165–168. doi:10.1016/j.matcom.2006.05.017.

[49] O. Malaspinas, Increasing stability and accuracy of the lattice Boltzmann scheme: recursivity and regularizationarXiv:1505.06900.

[50] D. Ricot, S. Marié, P. Sagaut, C. Bailly, Lattice Boltzmann method with selective viscosity filter, Journal of Computational Physics 228 (12) (2009) 4478–4490. doi:10.1016/j.jcp.2009.03.030.

[51] S. Marié, X. Gloerfelt, Adaptive filtering for the lattice Boltzmann method, Journal of Computational Physics 333 (2017) 212–226. doi:10.1016/j.jcp.2016.12.017.

[52] Y. Feng, P. Boivin, J. Jacob, P. Sagaut, Hybrid recursive regularized thermal lattice Boltzmann model for high subsonic compressible flows, Journal of Computational Physics 394 (2019) 82–99. doi:10.1016/j.jcp.2019.05.031.

[53] G. Wissocq, P. Sagaut, Hydrodynamic limits and numerical errors of isothermal lattice Boltzmann schemes, Journal of Computational Physics 450 (2022) 110858. doi:10.1016/J.JCP.2021.110858.

[54] A. D. Pierce, Acoustics - An Introduction to Its Physical Principles and Applications, Springer International Publishing, 2019. doi:10.1007/978-3-030-11214-1.

[55] F. J. Alexander, S. Chen, J. D. Sterling, Lattice Boltzmann thermohydrodynamics, Physical Review E 47 (4) (1993) R2249. arXiv:9304006, doi:10.1103/PhysRevE.47.R2249.

[56] X. He, S. Chen, G. D. Doolen, A Novel Thermal Model for the Lattice Boltzmann Method in Incompressible Limit, Journal of Computational Physics 146 (1) (1998) 282–300. doi:10.1006/JCPH.1998.6057.

[57] P. Lallemand, L. S. Luo, Hybrid Finite-Difference Thermal Lattice Boltzmann Equation, International Journal of Modern

Physics B 17 (1-2) (2003) 41–47. doi:10.1142/S0217979203017060.

[58] P. A. Skordos, Initial and boundary conditions for the lattice Boltzmann method, Physical Review E 48 (6) (1993) 4823–4842. doi:10.1103/PhysRevE.48.4823.

[59] P. van Leemput, C. Vandekerckhove, W. Vanroose, D. Roose, Accuracy of Hybrid Lattice Boltzmann/Finite Difference Schemes for Reaction-Diffusion Systems, Multiscale Modeling & Simulation 6 (3) (2007) 838–857. doi:10.1137/060675113.

[60] N. Yeshala, L. N. Sankar, Boundary condition implementation for a coupled lattice Boltzmann and Navier-Stokes methodology, in: 48th AIAA Aerospace Sciences Meeting Including the New Horizons Forum and Aerospace Exposition, American Institute of Aeronautics and Astronautics Inc., 2010. doi:10.2514/6.2010-715.

[61] S. Pawar, S. E. Ahmed, O. San, Interface learning in fluid dynamics: Statistical inference of closures within micro-macro-coupling models, Physics of Fluids 32 (9) (2020) 091704. arXiv:2008.04490, doi:10.1063/5.0024670.

[62] F. Gendre, D. Ricot, G. Fritz, P. Sagaut, Grid refinement for aeroacoustics in the lattice Boltzmann method: A directional splitting approach, Physical Review E 96 (2) (2017) 023311. doi:10.1103/PhysRevE.96.023311.

[63] G. Wissocq, J.-F. Boussuge, P. Sagaut, Consistent vortex initialization for the athermal lattice Boltzmann method, Physical Review E 101 (4) (2020) 043306. doi:10.1103/PhysRevE.101.043306.

[64] T. Krueger, H. Kusumaatmaja, A. Kuzmin, O. Shardt, G. Silva, E. M. Viggen, The Lattice Boltzmann Method: Principles and Practice, Graduate Texts in Physics, Springer, 2016.

[65] http://www.prolb-cfd.com/.

[66] O. Inoue, N. Hatakeyama, Sound generation by a two-dimensional circular cylinder in a uniform flow, Journal of Fluid Mechanics 471 (2002) 285–314. doi:10.1017/S0022112002002124.

[67] J. Robichaux, S. Balachandar, S. P. Vanka, Three-dimensional Floquet instability of the wake of square cylinder, Physics of Fluids 11 (2-3) (1999) 560–578. doi:10.1063/1.869930.

[68] K. W. Thompson, Time dependent boundary conditions for hyperbolic systems, Journal of Computational Physics 68 (1) (1987) 1–24. doi:10.1016/0021-9991(87)90041-6.

[69] J. T. Horstmann, T. Le Garrec, D. C. Mincu, E. Lévêque, Hybrid simulation combining two space–time discretization of the discrete-velocity Boltzmann equation, Journal of Computational Physics 349 (2017) 399–414. doi:10.1016/J.JCP.2017.08.029.

[70] G. D. Ilio, B. Dorschner, G. Bella, S. Succi, I. V. Karlin, Simulation of turbulent flows with the entropic multirelaxation time lattice Boltzmann method on body-fitted meshes, Journal of Fluid Mechanics 849 (2018) 35–56. doi:10.1017/JFM.2018.413.

[71] T. Astoul, G. Wissocq, J.-F. Boussuge, A. Sengissen, P. Sagaut, Analysis and reduction of spurious noise generated at grid refinement interfaces with the lattice Boltzmann method, Journal of Computational Physics 418 (2020) 109645. doi:10.1016/j.jcp.2020.109645.

[72] A. Lafitte, F. Pérot, Investigation of the noise generated by cylinder flows using a direct Lattice-Boltzmann approach, in: 15th AIAA/CEAS Aeroacoustics Conference (30th AIAA Aeroacoustics Conference), American Institute of Aeronautics and Astronautics Inc., 2009. doi:10.2514/6.2009-3268.

[73] G. Jeanmasson, I. Mary, L. Mieussens, On some explicit local time stepping finite volume schemes for CFD, Journal of Computational Physics 397 (2019) 108818. doi:10.1016/j.jcp.2019.07.017.

[74] S. Chapman, T. G. Cowling, The Mathematical Theory of Non-uniform Gases: An Account of the Kinetic Theory of Viscosity, Thermal Conduction and Diffusion in Gases, Cambridge Mathematical Library, Cambridge University Press, 1990.

[75] H. Grad, Note on N-dimensional hermite polynomials, Communications on Pure and Applied Mathematics 2 (4) (1949) 325–330. doi:10.1002/cpa.3160020402.